A FINITE ELEMENT METHOD FOR HYPERBOLIC METAMATERIALS WITH APPLICATIONS FOR HYPERLENS*

FUHAO LIU†, WEI YANG‡, AND JICHUN LI§

Abstract. In this paper, we first derive a time-dependent Maxwell's equation model for simulating wave propagation in anisotropic dispersive media and hyperbolic metamaterials. The modeling equations are obtained by using the Drude-Lorentz model to approximate both the permittivity and permeability. Then we develop a time-domain finite element method and prove its discrete stability and optimal error estimate. This mathematical model and the proposed numerical method can be used to design effective hyperbolic superlenses by the dielectric-metal multilayer metamaterials in different frequency ranges. Extensive two-dimensional (2D) and 3D numerical results are presented to demonstrate the good performance of many 2D and 3D hyperbolic superlenses in different frequency ranges. This is the first finite element paper on solving the hyperbolic metamaterials in a time domain.

Key words. Maxwell's equations, mixed finite element method, hyperbolic metamaterials, Drude–Lorentz model, hyperlens

MSC codes. 65M60, 65M12, 78M10

DOI. 10.1137/23M1591207

1. Introduction. Hyperbolic metamaterials (HMMs) [14] are a class of uniaxial anisotropic electromagnetic materials which satisfy a hyperbolic (or indefinite) dispersion relation reflected by their indefinite permittivity and/or permeability tensors. Hence, they are also called indefinite metamaterials [38]. For example, for a three-dimensional (3D) relative permittivity ε_r and/or permeability tensors μ_r ,

(1.1)
$$\varepsilon_r = \begin{bmatrix} \epsilon_{\parallel} & 0 & 0 \\ 0 & \epsilon_{\perp} & 0 \\ 0 & 0 & \epsilon_{\perp} \end{bmatrix}, \quad \mu_r = \begin{bmatrix} \mu_{\parallel} & 0 & 0 \\ 0 & \mu_{\perp} & 0 \\ 0 & 0 & \mu_{\perp} \end{bmatrix},$$

it holds that

(1.2)
$$\epsilon_{\parallel} \cdot \epsilon_{\perp} < 0 \quad \text{and/or} \quad \mu_{\parallel} \cdot \mu_{\perp} < 0.$$

Here the subscripts \parallel and \perp denote the components parallel and perpendicular to the optical axis which is oriented along the x_1 -direction. In the 2D case, ε_r and μ_r become as

$$\varepsilon_r = \begin{bmatrix} \epsilon_{\parallel} & 0 \\ 0 & \epsilon_{\perp} \end{bmatrix}, \quad \mu_r = \begin{bmatrix} \mu_{\parallel} & 0 \\ 0 & \mu_{\perp} \end{bmatrix},$$

https://doi.org/10.1137/23M1591207

Funding: This work is partially supported by the Hunan Outstanding Youth Fund (2022JJ10043), NSFC Projects 12171411, National Key Research and Development Program of China (2023YFA1009100), and NSF grant DMS-2011943.

†School of Mathematics and Computational Science, Xiangtan University, Xiangtan, 411105, Hunan, People's Republic of China (liufuhaoedu@163.com).

[‡]Hunan Key Laboratory for Computation and Simulation in Science and Engineering, Xiangtan University, Xiangtan, 411105, Hunan, People's Republic of China (yangweixtu@126.com).

§Department of Mathematical Sciences, University of Nevada Las Vegas, Las Vegas, NV 89154-4020 USA (jichun.li@unlv.edu).

^{*}Received by the editors August 1, 2023; accepted for publication (in revised form) March 13, 2024; published electronically June 17, 2024.

while (1.2) still holds true. HMMs were initially used to fabricate lenses to achieve superresolution imaging [36, 41, 18, 35, 34, 20]. After more than ten years of development and exploration, researchers have extended the applications of HMMs to nanolithography [37], collimation, splitting, enhancing the spontaneous-emission, designing ultrasmall optical cavities, etc. More details can be found in recent review papers [14], where the authors list some schemes to design HMMs and their interesting applications.

Although there exist some hyperbolic materials in nature, such as graphite [38] in the wavelength range 240–280 nm, magnesium diboride (MgB_2) [38] in the frequency range higher than 627 THz, hexagonal boron nitride in midinfrared [6], etc., it is still difficult to use natural hyperbolic materials to fabricate functional devices that meet the requirements and achieve hyperbolic dispersion effects in specific frequency ranges. In order to create HMMs, we must make the permittivity (and/or permeability) negative in one or both directions. Currently, there are two artificial structures that exhibit this extreme anisotropy: (i) multilayers [41, 18, 35, 34] formed by alternately stacking subwavelength-thick dielectric and metal films and (ii) nanowire arrays [36] formed by embedding nanoscale metal wires in dielectric. Since there are few magnetic materials in nature, and it is much more difficult to control permeability than permittivity, most of the research on HMMs is based on adjusting a material's permittivity to make artificial materials exhibit a hyperbolic dispersion property. There are very few studies on HMMs obtained by adjusting the permeability [19].

Due to the relatively high cost of manufacturing metamaterials and physical experiments, numerical simulation plays an important role in the design of metamaterials and its applications. In many applications, we are concerned about the multifrequency properties of metamaterials, and hence time-domain algorithms are needed for simulation of HMMs. Two of the most popular time-domain numerical methods for electromagnetic materials are the time-domain finite element (FETD) method and time-domain finite difference (FDTD) method. Over the years, many excellent finite element methods have been proposed for solving Maxwell's equations in various electromagnetic media (e.g., the papers [1, 4, 8, 12, 17, 23, 7, 40], review paper [16], and monographs [29, 11, 22]). Due to our interest and expertise in finite element methods [21, 24] and their advantage in handling problems with complex geometries, we will consider the FETD method here.

Up until now, most of the research on HMMs has focused on how to design HMMs and use the commercial software COMSOL Multiphysics to study their singlefrequency properties [20, 37], but not on their multifrequency properties. There are very few FETD methods developed to simulate multifrequency wave propagation in HMMs. According to [32], we know that at high frequencies (part of the visible light band and ultraviolet band), the Drude model has a poor approximation effect on the physical properties of metals. The popular dispersion medium models used for metals interacting with high-frequency waves are mostly the Drude model and/or Lorentz model, and they are widely used in the study of electromagnetic metamaterials [22]. Moreover, most of these time-domain models are based on isotropic metamaterials [22] and on a single Drude or Lorentz model. In 2013, [9] used COMSOL Multiphysics 3.5 and a Drude-Lorentz (D-L) model [32] to achieve 100 nm resolution by using an incident wave with 405 nm wavelength. There are a few FDTD methods for approximating the permittivity by using mixed dispersion models (e.g., [44]). Finally, we would like to mention that though there are so many investigations of HMMs in the physics and engineering communities, there exist very limited mathematical analyses of HMMs and robust analyses of numerical methods for solving HMM models. In 2021, Lin [26] presented an adaptive boundary element method for a transmission problem with 2D HMMs in the frequency domain. In 2022, Ciarlet and Kachanovska [10] established a well-posedness and regularity result for a 2D HMM in the frequency domain. In the time-dependent case we are unaware of any numerical analysis for HMMs. Therefore, it is interesting to develop and analyze a time-domain finite element method to solve a time domain HMMs model, which is one of the main contributions of this paper.

Below are some Sobolev spaces we will use in this paper (cf. [29]):

$$H(curl;\Omega) = \{ \boldsymbol{v} \in (L^2(\Omega))^3 : \nabla \times \boldsymbol{v} \in (L^2(\Omega))^3 \},$$

$$H^{\alpha}(curl;\Omega) = \{ \boldsymbol{v} \in (H^{\alpha}(\Omega))^3 : \nabla \times \boldsymbol{v} \in (H^{\alpha}(\Omega))^3 \},$$

$$H_0(curl;\Omega) = \{ \boldsymbol{v} \in H(curl;\Omega) : \boldsymbol{n} \times \boldsymbol{v} = 0 \text{ on } \partial\Omega \},$$

where $H^{\alpha}(\Omega) = W^{\alpha,2}(\Omega)$ for any $\alpha \geq 0$, and Ω is assumed to be a simply connected Lipschitz domain in \mathbb{R}^3 , with boundary $\partial\Omega$ and unit normal vectors \boldsymbol{n} . The norms of $H(curl;\Omega)$ and $H^{\alpha}(curl;\Omega)$ are given by

$$\|m{v}\|_{H(curl;\Omega)} = \left(\|m{v}\|_{(L^2(\Omega))^3}^2 + \|
abla imes m{v}\|_{(L^2(\Omega))^3}^2\right)^{\frac{1}{2}},$$
 $\|m{v}\|_{H^{lpha}(curl;\Omega)} = \left(\|m{v}\|_{(H^{lpha}(\Omega))^3}^2 + \|
abla imes m{v}\|_{(H^{lpha}(\Omega))^3}^2\right)^{\frac{1}{2}}.$

We will also use the following norms: $\|\boldsymbol{v}\|_0 = \|\boldsymbol{v}\|_{(L^2(\Omega))^3}$, $\|\boldsymbol{v}\|_{\alpha,curl} = \|\boldsymbol{v}\|_{H^{\alpha}(curl;\Omega)}$, and $|\boldsymbol{v}|_{curl} = \|\nabla \times \boldsymbol{v}\|_0$. Note that when $\alpha = 0$, we have $H^{\alpha}(\Omega) = L^2(\Omega)$ and $H^{\alpha}(curl;\Omega) = H(curl;\Omega)$.

The rest of the paper is organized as follows. In section 2, we first derive the governing equations for simulating the wave propagation in a general anisotropic dispersive medium by using the D-L dispersion model. Then we establish an energy identity and the stability. In section 3, we propose a fully discrete finite element scheme for solving the system of our modelling equations. In section 4, we prove the discrete stability of our scheme. Section 5 is devoted to the optimal error analysis of our scheme. In section 6, we develop a uniaxial anisotropic perfectly match layer (APML) model to simulate the wave propagation in HMMs. In section 7, we present extensive numerical results to justify the optimal error analysis for our proposed scheme in the 3D case and simulate many interesting wave propagation phenomena that happened in the ideal HMM. We also present simulations of imaging in multiple groups of dielectric-metal multilayers lenses and demonstrate designs of some hyperbolic lenses in different wavelength ranges. We conclude the paper in section 8.

2. The system of modeling equations and its analysis. To derive the governing equations of the D-L model used for the simulation of hyperlens, we start from the standard time-harmonic Maxwell's equations (assuming $e^{j\omega t}$ dependence):

$$j\omega\widehat{\boldsymbol{B}} = -\nabla\times\widehat{\boldsymbol{E}}, \quad j\omega\widehat{\boldsymbol{D}} = \nabla\times\widehat{\boldsymbol{H}},$$

where \widehat{B} , \widehat{H} , \widehat{D} , and \widehat{E} are the magnetic flux density, magnetic field, electric flux density, and electric field, respectively. The constitutive relations between \widehat{D} and \widehat{B} and \widehat{E} and \widehat{H} in general linear dispersive media are

(2.1)
$$\widehat{\boldsymbol{D}} = \varepsilon_0 \boldsymbol{\varepsilon}_r(\omega) \widehat{\boldsymbol{E}}, \quad \widehat{\boldsymbol{B}} = \mu_0 \boldsymbol{\mu}_r(\omega) \widehat{\boldsymbol{H}},$$

where ε_0 and μ_0 are the vacuum permittivity and permeability, $j = \sqrt{-1}$, ω denotes the wave frequency, and tensors ε_r , μ_r denote the relative permittivity and permeability of the underlying media.

In this paper, we assume that ε_r and μ_r are diagonal matrices represented as $\boldsymbol{\varepsilon}_r = \operatorname{diag}(\varepsilon_x, \varepsilon_y, \varepsilon_z)$ and $\boldsymbol{\mu}_r = \operatorname{diag}(\mu_x, \mu_y, \mu_z)$. For the D-L model, we have

(2.2)
$$\boldsymbol{\varepsilon}_r = \boldsymbol{\varepsilon}_{\infty} + \sum_{q=0}^{Q} \boldsymbol{f}_q \boldsymbol{\chi}_{eq}(\omega), \quad \boldsymbol{\mu}_r = \boldsymbol{\mu}_{\infty} + \sum_{l=0}^{L} \boldsymbol{g}_l \boldsymbol{\chi}_{ml}(\omega),$$

where ε_{∞} and μ_{∞} are positive definite diagonal matrices and denote the relative permeability and permittivity at infinite frequency, and $\sum_{q=0}^{Q} f_q \chi_{eq}(\omega)$ and $\sum_{l=0}^{L} g_l \chi_{ml}(\omega)$ denote electric and magnetic susceptibilities, respectively. Furthermore, we denote

$$(2.3) \quad \boldsymbol{f}_{q} = \operatorname{diag}(f_{q,x}, f_{q,y}, f_{q,z}), \quad \boldsymbol{g}_{l} = \operatorname{diag}(g_{l,x}, g_{l,y}, g_{l,z}), \quad f_{q,i} > 0, \quad g_{l,i} \ge 0, \quad i = x, y, z,$$

$$(2.4) \quad \boldsymbol{\chi}_{eq} = \operatorname{diag}(\chi_{eq,x}, \chi_{eq,y}, \chi_{eq,z}), \quad \boldsymbol{\chi}_{ml} = \operatorname{diag}(\chi_{ml,x}, \chi_{ml,y}, \chi_{ml,z}),$$

where $\chi_{eq,i}(\omega) = \frac{\omega_{p,i}^2}{\omega_{eq,i}^2 + (j\omega)^2 + j\omega\Gamma_{eq,i}}, \ \chi_{ml,i}(\omega) = \frac{\omega_{m,i}^2}{\omega_{ml,i}^2 + (j\omega)^2 + j\omega\Gamma_{ml,i}}$ with $\omega_{p,i}, \omega_{m,i} > 0$ and $\omega_{eq,i}, \Gamma_{eq,i}, \ \omega_{ml,i}, \Gamma_{ml,i} \geq 0$ for all i = x, y, z.

Let us introduce

(2.5)
$$\widehat{\boldsymbol{P}}_{q} = \boldsymbol{\chi}_{eq}(\omega)\widehat{\boldsymbol{E}}, \quad \widehat{\boldsymbol{M}}_{l} = \boldsymbol{\chi}_{ml}(\omega)\widehat{\boldsymbol{H}}.$$

Applying the inverse Fourier transform (cf. [22]) to (2.5), we obtain

(2.6)
$$\partial_{tt} \mathbf{P}_q + \Gamma_{eq} \partial_t \mathbf{P}_q + \omega_{eq}^2 \mathbf{P}_q = \omega_p^2 \mathbf{E}, \quad q = 0, 1, 2, \dots, Q,$$

(2.7)
$$\partial_{tt} \mathbf{M}_l + \mathbf{\Gamma}_{ml} \partial_t \mathbf{M}_l + \boldsymbol{\omega}_{ml}^2 \mathbf{M}_l = \boldsymbol{\omega}_m^2 \mathbf{H}, \quad l = 0, 1, 2, \dots, L.$$

Introducing auxiliary variables $J_q = \partial_t P_q$ and $K_l = \partial_t M_l$, and using (2.6)–(2.7), we obtain the time-domain D-L model given as

(2.8a)
$$\varepsilon_0 \boldsymbol{\varepsilon}_{\infty} \partial_t \boldsymbol{E} + \varepsilon_0 \sum_{q=0}^{Q} \boldsymbol{f}_q \boldsymbol{J}_q = \nabla \times \boldsymbol{H},$$

(2.8b)
$$\partial_t \boldsymbol{J}_q + \boldsymbol{\Gamma}_{eq} \boldsymbol{J}_q = \boldsymbol{\omega}_p^2 \boldsymbol{E} - \boldsymbol{\omega}_{eq}^2 \boldsymbol{P}_q, \quad q = 0, 1, \dots, Q,$$
(2.8c)
$$\partial_t \boldsymbol{P}_q = \boldsymbol{J}_q, \qquad q = 0, 1, \dots, Q,$$

$$(2.8c) \partial_t \boldsymbol{P}_q = \boldsymbol{J}_q, q = 0, 1, \dots, Q,$$

(2.8d)
$$\mu_0 \boldsymbol{\mu}_{\infty} \partial_t \boldsymbol{H} + \mu_0 \sum_{l=0}^{L} \boldsymbol{g}_l \boldsymbol{K}_l = -\nabla \times \boldsymbol{E},$$

(2.8e)
$$\partial_t \mathbf{K}_l + \mathbf{\Gamma}_{ml} \mathbf{K}_l = \boldsymbol{\omega}_m^2 \mathbf{H} - \boldsymbol{\omega}_{ml}^2 \mathbf{M}_l, \ l = 0, 1, \dots, L,$$

$$(2.8f) \partial_t \mathbf{M}_l = \mathbf{K}_l, l = 0, 1, \dots, L.$$

To complete the model, we assume that (2.8a)-(2.8f) are subject to the perfect electric conductor (PEC) boundary condition,

(2.9)
$$\mathbf{n} \times \mathbf{E} = 0 \text{ on } \partial \Omega$$

and the following initial conditions:

(2.10)
$$E(x;0) = E^{0}(x), \quad J_{q}(x;0) = J_{q}^{0}(x), \quad P_{q}(x;0) = P_{q}^{0}(x),$$

$$H(x;0) = H^{0}(x), \quad K_{l}(x;0) = K_{l}^{0}(x), \quad M_{l}(x;0) = M_{l}^{0}(x),$$

where $E^0(x)$, $J_q^0(x)$, $P_q^0(x)$, $H^0(x)$, $K_l^0(x)$, $M_l^0(x)$ are some given functions in Ω . We would like to remark that introducing auxiliary variables J_q and K_l above is a common method adopted for modeling dispersive media. This technique started

in the early 1990s (early references can be found in the book by Taflove and Hagness [39]) and has been used in analysis and simulation of various dispersive media in both FDTD and finite element methods (e.g., [3, 5, 25, 28, 31] and references therein).

Denote $U = (L^2(\Omega))^3$, $V = H(curl; \Omega)$, $V_0 = H_0(curl; \Omega)$. We can obtain the following weak formulation of (2.8a)–(2.8f): Find E, J_q , $P_q \in H^1(0,T; V_0) \cap L^2(0,T; V_0)$ and H, K_l , $M_l \in H^1(0,T; U) \cap L^2(0,T; U)$ such that

(2.11a)
$$\varepsilon_0(\boldsymbol{\varepsilon}_{\infty}\partial_t \boldsymbol{E}, \boldsymbol{\psi}) + \varepsilon_0 \sum_{q=0}^{Q} (\boldsymbol{f}_q \boldsymbol{J}_q, \boldsymbol{\psi}) = (\boldsymbol{H}, \nabla \times \boldsymbol{\psi}),$$

$$(2.11b) (A_q \partial_t \boldsymbol{J}_q, \boldsymbol{\psi}_q) + (A_q \boldsymbol{\Gamma}_{eq} \boldsymbol{J}_q, \boldsymbol{\psi}_q) = (\boldsymbol{f}_q \boldsymbol{E}, \boldsymbol{\psi}_q) - (A_q \boldsymbol{\omega}_{eq}^2 \boldsymbol{P}_q, \boldsymbol{\psi}_q),$$

(2.11c)
$$(\partial_t \boldsymbol{P}_q, \tilde{\boldsymbol{\psi}}_q) = (\boldsymbol{J}_q, \tilde{\boldsymbol{\psi}}_q),$$

(2.11d)
$$\mu_0(\boldsymbol{\mu}_{\infty}\partial_t \boldsymbol{H}, \boldsymbol{\varphi}) + \mu_0 \sum_{l=0}^{L} (\boldsymbol{g}_l \boldsymbol{K}_l, \boldsymbol{\varphi}) = -(\nabla \times \boldsymbol{E}, \boldsymbol{\varphi}),$$

(2.11e)
$$(\partial_t \mathbf{K}_l, \varphi_l) + (\mathbf{\Gamma}_{ml} \mathbf{K}_l, \varphi_l) = (\omega_m^2 \mathbf{H}, \varphi_l) - (\omega_{ml}^2 \mathbf{M}_l, \varphi_l),$$

(2.11f)
$$(\partial_t \boldsymbol{M}_l, \tilde{\boldsymbol{\varphi}}_l) = (\boldsymbol{K}_l, \tilde{\boldsymbol{\varphi}}_l)$$

hold true for any $\psi \in V_0$, $\psi_q, \tilde{\psi}_q \in V$, $\varphi, \varphi_l, \tilde{\varphi}_l \in U$, q = 0, 1, ..., Q, l = 0, 1, ..., L. We would like to remark that (2.11b) is obtained by multiplying (2.8b) with matrix $A_q := \omega_p^{-2} f_q$, which is positive definite.

Below we will use the weighted L^2 norm notation $\|u\|_A = \sqrt{(u, Au)}$ for any diagonal matrix $A = \text{diag}(a_1, a_2, a_3)$ with $a_i \ge 0, i = 1, 2, 3$. We will also denote the following constant coefficient matrices

$$C_q := \boldsymbol{\omega}_{eq}^2 \boldsymbol{\omega}_p^{-2} \boldsymbol{f}_q, \ \tilde{A}_l := \boldsymbol{\omega}_m^{-2} \boldsymbol{g}_l, \ \tilde{C}_l := \boldsymbol{\omega}_{ml}^2 \boldsymbol{\omega}_m^{-2} \boldsymbol{g}_l.$$

Theorem 2.1. For any $t \in (0,T]$, the solution $(E, J_q, P_q, H, K_l, M_l)$ to (2.11) satisfies the energy identity

$$\begin{split} \frac{d}{dt} \left[\varepsilon_{0} \| \boldsymbol{E} \|_{\varepsilon_{\infty}}^{2} + \varepsilon_{0} \sum_{q=0}^{Q} \left(\| \boldsymbol{J}_{q} \|_{A_{q}}^{2} + \| \boldsymbol{P}_{q} \|_{C_{q}}^{2} \right) + \mu_{0} \| \boldsymbol{H} \|_{\boldsymbol{\mu}_{\infty}}^{2} + \mu_{0} \sum_{l=0}^{L} \left(\| \boldsymbol{K}_{l} \|_{\tilde{A}_{l}}^{2} + \| \boldsymbol{M}_{l} \|_{\tilde{C}_{l}}^{2} \right) \right] \\ + 2\varepsilon_{0} \sum_{q=0}^{Q} \| \boldsymbol{J}_{q} \|_{\boldsymbol{\Gamma}_{eq}A_{q}}^{2} + 2\mu_{0} \sum_{l=0}^{L} \| \boldsymbol{K}_{l} \|_{\boldsymbol{\Gamma}_{ml}\tilde{A}_{l}}^{2} = 0 \end{split}$$

and the stability

(2.13)
$$\epsilon_{0} \|\boldsymbol{E}(t)\|_{\boldsymbol{\varepsilon}_{\infty}}^{2} + \varepsilon_{0} \sum_{q=0}^{Q} \left(\|\boldsymbol{J}_{q}(t)\|_{A_{q}}^{2} + \|\boldsymbol{P}_{q}(t)\|_{C_{q}}^{2} \right) \\ + \mu_{0} \|\boldsymbol{H}(t)\|_{\boldsymbol{\mu}_{\infty}}^{2} + \mu_{0} \sum_{l=0}^{L} \left(\|\boldsymbol{K}_{l}(t)\|_{\tilde{A}_{l}}^{2} + \|\boldsymbol{M}_{l}(t)\|_{\tilde{C}_{l}}^{2} \right) \\ \leq \varepsilon_{0} \|\boldsymbol{E}(0)\|_{\boldsymbol{\varepsilon}_{\infty}}^{2} + \varepsilon_{0} \sum_{q=0}^{Q} \left(\|\boldsymbol{J}_{q}(0)\|_{A_{q}}^{2} + \|\boldsymbol{P}_{q}(t)\|_{C_{q}}^{2} \right) \\ + \mu_{0} \|\boldsymbol{H}(0)\|_{\boldsymbol{\mu}_{\infty}}^{2} + \mu_{0} \sum_{l=0}^{L} \left(\|\boldsymbol{K}_{l}(0)\|_{\tilde{A}_{l}}^{2} + \|\boldsymbol{M}_{l}(0)\|_{\tilde{C}_{l}}^{2} \right).$$

Proof. Letting $\varphi = H$ and $\psi = E$ in (2.11d) and (2.11a), respectively, then adding the results together, we have

$$(2.14) \quad \mu_0(\boldsymbol{\mu}_{\infty}\partial_t\boldsymbol{H},\boldsymbol{H}) + \mu_0 \sum_{l=0}^{L} (\boldsymbol{g}_l\boldsymbol{K}_l,\boldsymbol{H}) + \varepsilon_0(\boldsymbol{\varepsilon}_{\infty}\partial_t\boldsymbol{E},\boldsymbol{E}) + \varepsilon_0 \sum_{q=0}^{Q} (\boldsymbol{f}_q\boldsymbol{J}_q,\boldsymbol{E}) = 0.$$

Taking $\boldsymbol{\psi}_q = \boldsymbol{J}_q$, $\tilde{\boldsymbol{\psi}}_q = C_q \boldsymbol{P}_q$, $\boldsymbol{\varphi}_l = \tilde{A}_l \boldsymbol{K}_l$, $\tilde{\boldsymbol{\varphi}}_l = \tilde{C}_l \boldsymbol{M}_l$ in (2.11b), (2.11c), (2.11e), and (2.11f), respectively, we have

$$(2.15a) (A_q \partial_t \boldsymbol{J}_q, \boldsymbol{J}_q) + (A_q \boldsymbol{\Gamma}_{eq} \boldsymbol{J}_q, \boldsymbol{J}_q) = (\boldsymbol{f}_q \boldsymbol{E}, \boldsymbol{J}_q) - (A_q \boldsymbol{\omega}_{eq}^2 \boldsymbol{P}_q, \boldsymbol{J}_q),$$

(2.15b)
$$(\partial_t \mathbf{P}_q, C_q \mathbf{P}_q) = (\mathbf{J}_q, C_q \mathbf{P}_q),$$

(2.15c)
$$(\partial_t \mathbf{K}_l, \tilde{A}_l \mathbf{K}_l) + (\mathbf{\Gamma}_{ml} \mathbf{K}_l, \tilde{A}_l \mathbf{K}_l) = (\mathbf{H}, \mathbf{g}_l \mathbf{K}_l) - (\boldsymbol{\omega}_{ml}^2 \mathbf{M}_l, \tilde{A}_l \mathbf{K}_l),$$

(2.15d)
$$(\partial_t \mathbf{M}_l, \tilde{C}_l \mathbf{M}_l) = (\mathbf{K}_l, \tilde{C}_l \mathbf{M}_l).$$

Adding (2.15a) and (2.15c) to (2.15b) and (2.15d), respectively, and using the facts $C_q = \omega_{eq}^2 A_q$, $\tilde{C}_l = \omega_{ml}^2 \tilde{A}_l$, we obtain

(2.16a)
$$\frac{1}{2} \frac{d}{dt} \left[\| \boldsymbol{J}_q \|_{A_q}^2 + \| \boldsymbol{P}_q \|_{C_q}^2 \right] + \| \boldsymbol{J}_q \|_{\Gamma_{eq} A_q}^2 = (\boldsymbol{E}, \boldsymbol{f}_q \boldsymbol{J}_q),$$

(2.16b)
$$\frac{1}{2} \frac{d}{dt} \left[\| \mathbf{K}_l \|_{\tilde{A}_l}^2 + \| \mathbf{M}_l \|_{\tilde{C}_l}^2 \right] + \| \mathbf{K}_l \|_{\mathbf{\Gamma}_{ml}\tilde{A}_l}^2 = (\mathbf{H}, \mathbf{g}_l \mathbf{K}_l).$$

Substituting (2.16) into (2.14), we complete the proof of (2.12).

Dropping the last two nonnegative terms on the left-hand side of (2.12), then integrating the result from 0 to t, we immediately prove (2.13).

3. A fully discrete finite element scheme. To develop a finite element scheme, we partition the physical domain Ω by a family of regular tetrahedral mesh T_h with maximal mesh size h. Considering the low regularity of the solution to Maxwell's equations in complex media and its simplicity in implementation, we just choose the lowest-order Raviart-Thomas-Nédélec (RTN) mixed finite element spaces [33, 30, 29]:

$$\begin{aligned} & \boldsymbol{U}_h = \{\boldsymbol{u}_h \in (L^2(\Omega))^3: \ \boldsymbol{u}_h|_K \text{ is a piecewise constant, } K \in T_h\}, \\ & \boldsymbol{V}_h = \{\boldsymbol{v}_h \in \boldsymbol{H}(curl;\Omega): \ \boldsymbol{v}_h|_K = \boldsymbol{a} + \boldsymbol{b} \times \boldsymbol{x}, K \in T_h\}, \\ & \boldsymbol{V}_h^0 = \{\boldsymbol{v}_h \in \boldsymbol{V}_h: \boldsymbol{v}_h \times \boldsymbol{n} = \boldsymbol{0}, \text{ on } \partial \Omega\}, \end{aligned}$$

where the constant vectors $\boldsymbol{a}, \boldsymbol{b} \in \mathbb{R}^3$.

For the time interval [0,T], we divide it into N uniform subintervals by points $t_k = k\tau$, where $\tau = \frac{T}{N}$, and k = 0, 1, ..., N. For time-indexed solutions $\mathbf{u}^k = \mathbf{u}(\cdot, k\tau)$, we introduce the following central difference operator and averaging operator:

$$\delta_{ au}m{u}^k = rac{m{u}^{k+rac{1}{2}} - m{u}^{k-rac{1}{2}}}{ au}, \ m{\overline{u}}^{k+rac{1}{2}} = rac{m{u}^{k+1} + m{u}^k}{2}.$$

Now we propose the following leapfrog type scheme: Given proper initial approximations $\boldsymbol{E}_{h}^{0} \in \boldsymbol{V}_{h}^{0}, \, \boldsymbol{P}_{qh}^{0}, \boldsymbol{J}_{qh}^{\frac{1}{2}} \in \boldsymbol{V}_{h}, \, \boldsymbol{H}_{h}^{\frac{1}{2}}, \boldsymbol{M}_{lh}^{\frac{1}{2}}, \boldsymbol{K}_{lh}^{0} \in \boldsymbol{U}_{h}, \, \text{find } \boldsymbol{E}_{h}^{k+1} \in \boldsymbol{V}_{h}^{0}, \, \boldsymbol{J}_{qh}^{k+\frac{3}{2}}, \boldsymbol{P}_{qh}^{k+1} \in V_{h}, \, \boldsymbol{H}_{h}^{k+\frac{3}{2}}, \boldsymbol{M}_{lh}^{k+\frac{3}{2}}, \boldsymbol{K}_{lh}^{k+1} \in \boldsymbol{U}_{h}, \, \text{such that}$

(3.1a)
$$\varepsilon_0(\boldsymbol{\varepsilon}_{\infty}\delta_{\tau}\boldsymbol{E}_h^{k+\frac{1}{2}},\boldsymbol{\psi}_h) + \varepsilon_0 \sum_{q=0}^{Q} (\boldsymbol{f}_q \boldsymbol{J}_{qh}^{k+\frac{1}{2}},\boldsymbol{\psi}_h) - (\boldsymbol{H}_h^{k+\frac{1}{2}},\nabla\times\boldsymbol{\psi}_h) = 0,$$

(3.1b)
$$(\delta_{\tau} \boldsymbol{P}_{qh}^{k+\frac{1}{2}}, \tilde{\boldsymbol{\psi}}_{qh}) - (\boldsymbol{J}_{qh}^{k+\frac{1}{2}}, \tilde{\boldsymbol{\psi}}_{qh}) = 0,$$

$$(3.1c) \ \ (A_q \delta_\tau \boldsymbol{J}_{qh}^{k+1}, \boldsymbol{\psi}_{qh}) + (A_q \boldsymbol{\Gamma}_{eq} \overline{\boldsymbol{J}}_{qh}^{k+1}, \boldsymbol{\psi}_{qh}) - (\boldsymbol{f}_q \boldsymbol{E}_h^{k+1}, \boldsymbol{\psi}_{qh}) + (C_q \boldsymbol{P}_{qh}^{k+1}, \boldsymbol{\psi}_{qh}) = 0,$$

(3.1d)
$$(\delta_{\tau} \boldsymbol{K}_{lh}^{k+\frac{1}{2}}, \boldsymbol{\varphi}_{lh}) + (\boldsymbol{\Gamma}_{ml} \overline{\boldsymbol{K}}_{lh}^{k+\frac{1}{2}}, \boldsymbol{\varphi}_{lh}) - (\boldsymbol{\omega}_{m}^{2} \boldsymbol{H}_{h}^{k+\frac{1}{2}}, \boldsymbol{\varphi}_{lh}) + (\boldsymbol{\omega}_{ml}^{2} \boldsymbol{M}_{lh}^{k+\frac{1}{2}}, \boldsymbol{\varphi}_{lh}) = 0,$$

(3.1e) $(\delta_{\tau} \boldsymbol{M}_{lh}^{k+1}, \tilde{\boldsymbol{\varphi}}_{lh}) - (\boldsymbol{K}_{lh}^{k+1}, \tilde{\boldsymbol{\varphi}}_{lh}) = 0,$

(3.1e)
$$(\delta_{\tau} \boldsymbol{M}_{lh}^{k+1}, \tilde{\boldsymbol{\varphi}}_{lh}) - (\boldsymbol{K}_{lh}^{k+1}, \tilde{\boldsymbol{\varphi}}_{lh}) = 0$$

(3.1f)
$$\mu_0(\boldsymbol{\mu}_{\infty}\delta_{\tau}\boldsymbol{H}_h^{k+1},\boldsymbol{\varphi}_h) + \mu_0 \sum_{l=0}^{L} (\boldsymbol{g}_l \boldsymbol{K}_{lh}^{k+1},\boldsymbol{\varphi}_h) + (\nabla \times \boldsymbol{E}_h^{k+1},\boldsymbol{\varphi}_h) = 0$$

hold true for any $\psi_h \in V_h^0$, $\varphi_h, \varphi_{qh}, \tilde{\varphi}_{qh} \in U_h$, $\psi_{qh}, \tilde{\psi}_{qh} \in V_h$, $q = 0, 1, \dots, Q$,

Using the Nédélec interpolation operator r_h [29], $H^{\alpha}(curl;\Omega) \to V_h$, the L^2 projection operator $\boldsymbol{w}_h:(L^2(\Omega))^3\to\boldsymbol{U}_h$, Taylor expansion, and the modeling equations (2.8a)–(2.8f), we choose the following initial approximations for scheme (3.1):

$$(3.2a) \quad \boldsymbol{E}_{h}^{0} = \boldsymbol{r}_{h} \boldsymbol{E}^{0}, \ \boldsymbol{P}_{qh}^{0} = \boldsymbol{r}_{h} \boldsymbol{P}_{q}^{0}, \ \boldsymbol{J}_{qh}^{\frac{1}{2}} = \boldsymbol{r}_{h} \left[\boldsymbol{J}_{q}^{0} + \frac{\tau}{2} \left(\boldsymbol{\omega}_{p}^{2} \boldsymbol{E}^{0} - \boldsymbol{\omega}_{eq}^{2} \boldsymbol{P}_{q}^{0} - \boldsymbol{\Gamma}_{eq} \boldsymbol{J}_{q}^{0} \right) \right],$$

(3.2b)
$$\boldsymbol{H}_{h}^{\frac{1}{2}} = \boldsymbol{w}_{h} \left[\boldsymbol{H}^{0} - \frac{\tau}{2} \left(\mu_{\infty}^{-1} \sum_{l=0}^{L} \boldsymbol{g}_{l} \boldsymbol{K}_{l}^{0} + \mu_{0}^{-1} \mu_{\infty}^{-1} \nabla \times \boldsymbol{E}^{0} \right) \right],$$

(3.2c)
$$\boldsymbol{M}_{lh}^{\frac{1}{2}} = \boldsymbol{w}_h \left[\boldsymbol{M}_l^0 + \frac{\tau}{2} \boldsymbol{K}_l^0 \right], \, \boldsymbol{K}_{lh}^0 = \boldsymbol{w}_h \boldsymbol{K}_l^0.$$

The approximations (3.2a)–(3.2c) guarantee the following initial error estimates:

(3.3a)
$$\|\boldsymbol{E}_{h}^{0} - \boldsymbol{r}_{h} \boldsymbol{E}^{0}\|_{0} + \|\boldsymbol{P}_{qh}^{0} - \boldsymbol{P}_{q}^{0}\|_{0} + \|\boldsymbol{K}_{lh}^{0} - \boldsymbol{K}_{l}^{0}\|_{0} \leq Ch^{\alpha},$$

(3.3b)
$$\|\boldsymbol{J}_{qh}^{\frac{1}{2}} - \boldsymbol{J}_{q}^{\frac{1}{2}}\|_{0} + \|\boldsymbol{H}_{h}^{\frac{1}{2}} - \boldsymbol{H}^{\frac{1}{2}}\|_{0} + \|\boldsymbol{M}_{lh}^{\frac{1}{2}} - \boldsymbol{M}_{l}^{\frac{1}{2}}\|_{0} \le C(h^{\alpha} + \tau^{2}).$$

4. Stability analysis for our scheme. To prove the discrete stability and the convergence for our scheme, we need a projection operator Π_{qh} [42]: For any $P_{qh} \in V_h$, $\Pi_{qh} \boldsymbol{P}_{qh} \in V_h$ is the solution of

$$(\Pi_{qh} \boldsymbol{P}_{qh}, \boldsymbol{v}_h) = (C_q \boldsymbol{P}_{qh}, \boldsymbol{v}_h) \ \forall \boldsymbol{v}_h \in \boldsymbol{V}_h, \ q = 0, 1, \dots, Q.$$

Furthermore, we denote $C_v = \frac{1}{\sqrt{\mu_0 \varepsilon_0}}$ for the wave speed in vacuum, and the maximum matrix norm $||A||_{\infty} = \max_{1 \le i \le 3} |a_i|$ for any diagonal matrix $A = \operatorname{diag}(a_1, a_2, a_3)$.

In this section, we will prove the following discrete stability for our scheme.

Theorem 4.1. Denote constant $C_{inv} > 0$ in the standard inverse estimate

(4.1)
$$\|\nabla \times \boldsymbol{E}_h\|_0 \le C_{inv} h^{-1} \|\boldsymbol{E}_h\|_0 \ \forall \boldsymbol{E}_h \in \boldsymbol{V}_h.$$

If the time step τ satisfies

$$(4.2) \qquad \tau \leq \min \left\{ \frac{h}{2C_v C_{inv}}, \min_{0 \leq q \leq Q} \left(\frac{1}{2\|\boldsymbol{\omega}_{eq}\|_{\infty}}, \frac{1}{2\sqrt{Q+1}\|\boldsymbol{\omega}_{p}\boldsymbol{f}_{q}^{\frac{1}{2}}\|_{\infty}} \right), \right. \\ \left. \min_{0 \leq l \leq L} \left(\frac{1}{2\|\boldsymbol{\omega}_{ml}\|_{\infty}}, \frac{1}{2\sqrt{L+1}\|\boldsymbol{\omega}_{m}\boldsymbol{g}_{l}^{\frac{1}{2}}\|_{\infty}} \right) \right\},$$

then the solution $(\boldsymbol{E}_h^n, \boldsymbol{J}_{qh}^{n+\frac{1}{2}}, \boldsymbol{P}_{qh}^n, \boldsymbol{H}_h^{n+\frac{1}{2}}, \boldsymbol{M}_{lh}^{n+\frac{1}{2}}, \boldsymbol{K}_{lh}^n)$ of scheme (3.1) satisfies the following stability: For all $n \geq 1$,

$$\varepsilon_{0} \|\boldsymbol{E}_{h}^{n}\|_{\boldsymbol{\varepsilon}_{\infty}}^{2} + \varepsilon_{0} \sum_{q=0}^{Q} \left(\|\boldsymbol{J}_{qh}^{n+\frac{1}{2}}\|_{A_{q}}^{2} + \|\boldsymbol{P}_{qh}^{n}\|_{C_{q}}^{2} \right) \\
+ \mu_{0} \|\boldsymbol{H}_{h}^{n+\frac{1}{2}}\|_{\boldsymbol{\mu}_{\infty}}^{2} + \mu_{0} \sum_{l=0}^{L} \left(\|\boldsymbol{K}_{lh}^{n}\|_{\tilde{A}_{l}}^{2} + \|\boldsymbol{M}_{lh}^{n+\frac{1}{2}}\|_{\tilde{C}_{l}}^{2} \right) \\
\leq 3 \left[\varepsilon_{0} \|\boldsymbol{E}_{h}^{0}\|_{\boldsymbol{\varepsilon}_{\infty}}^{2} + \varepsilon_{0} \sum_{q=0}^{Q} \left(\|\boldsymbol{J}_{qh}^{\frac{1}{2}}\|_{A_{q}}^{2} + \|\boldsymbol{P}_{qh}^{0}\|_{C_{q}}^{2} \right) \\
+ \mu_{0} \|\boldsymbol{H}_{h}^{\frac{1}{2}}\|_{\boldsymbol{\mu}_{\infty}}^{2} + \mu_{0} \sum_{l=0}^{L} \left(\|\boldsymbol{K}_{lh}^{0}\|_{\tilde{A}_{l}}^{2} + \|\boldsymbol{M}_{lh}^{\frac{1}{2}}\|_{\tilde{C}_{l}}^{2} \right) \right].$$

Proof. To make our proof easy to follow, we divide it into three major parts. (I) Taking $\psi_h = 2\tau \overline{\boldsymbol{E}}_h^{k+\frac{1}{2}}$ and $\varphi_h = 2\tau \overline{\boldsymbol{H}}_h^{k+1}$ in (3.1a) and (3.1f), respectively, and adding the results together, we have

$$\varepsilon_{0}(\|\boldsymbol{E}_{h}^{k+1}\|_{\boldsymbol{\varepsilon}_{\infty}}^{2} - \|\boldsymbol{E}_{h}^{k}\|_{\boldsymbol{\varepsilon}_{\infty}}^{2}) + \mu_{0}(\|\boldsymbol{H}_{h}^{k+\frac{3}{2}}\|_{\boldsymbol{\mu}_{\infty}}^{2} - \|\boldsymbol{H}_{h}^{k+\frac{1}{2}}\|_{\boldsymbol{\mu}_{\infty}}^{2})$$

$$= \tau \left[(\nabla \times \boldsymbol{E}_{h}^{k}, \boldsymbol{H}_{h}^{k+\frac{1}{2}}) - (\nabla \times \boldsymbol{E}_{h}^{k+1}, \boldsymbol{H}_{h}^{k+\frac{3}{2}}) \right]$$

$$- 2\tau \mu_{0} \sum_{l=0}^{L} (\boldsymbol{g}_{l} \boldsymbol{K}_{lh}^{k+1}, \overline{\boldsymbol{H}}_{h}^{k+1}) - 2\tau \varepsilon_{0} \sum_{q=0}^{Q} (\boldsymbol{f}_{q} \boldsymbol{J}_{qh}^{k+\frac{1}{2}}, \overline{\boldsymbol{E}}_{h}^{k+\frac{1}{2}}).$$

Taking $\tilde{\boldsymbol{\psi}}_{qh} = 2\varepsilon_0 \tau \Pi_{qh} \overline{\boldsymbol{P}}_{qh}^{k+\frac{1}{2}}$ and $\boldsymbol{\psi}_{qh} = 2\tau \varepsilon_0 \overline{\boldsymbol{J}}_{qh}^{k+1}$ in (3.1b) and (3.1c), respectively, adding the results together, and dropping the nonnegative term $2\tau \varepsilon_0 (\boldsymbol{\Gamma}_{eq} \overline{\boldsymbol{J}}_{qh}^{k+1})$, $A_q \overline{\boldsymbol{J}}_{qh}^{k+1}$), we obtain

$$\begin{aligned}
&(4.5) \\
&\varepsilon_{0}(\|\boldsymbol{J}_{qh}^{k+\frac{3}{2}}\|_{A_{q}}^{2} - \|\boldsymbol{J}_{qh}^{k+\frac{1}{2}}\|_{A_{q}}^{2}) + \varepsilon_{0}(\|\boldsymbol{P}_{qh}^{k+1}\|_{C_{q}}^{2} - \|\boldsymbol{P}_{qh}^{k}\|_{C_{q}}^{2}) \\
&\leq \tau \varepsilon_{0}(\boldsymbol{E}_{h}^{k+1}, \boldsymbol{f}_{q}(\boldsymbol{J}_{qh}^{k+\frac{3}{2}} + \boldsymbol{J}_{qh}^{k+\frac{1}{2}})) + \tau \varepsilon_{0}\left[(C_{q}\boldsymbol{J}_{qh}^{k+\frac{1}{2}}, \boldsymbol{P}_{qh}^{k}) - (C_{q}\boldsymbol{J}_{qh}^{k+\frac{3}{2}}, \boldsymbol{P}_{qh}^{k+1}) \right].
\end{aligned}$$

Similarly, taking $\varphi_{lh} = 2\mu_0 \tau \tilde{A}_l \overline{K}_{lh}^{k+\frac{1}{2}}$ and $\tilde{\varphi}_{lh} = 2\mu_0 \tau \tilde{C}_l \overline{M}_{lh}^{k+1}$ in (3.1d) and (3.1e), respectively, and adding the results together, we obtain

(II) Now, summing up (4.5) over q = 0, 1, ..., Q, and (4.6) over l = 0, 1, ..., L, respectively, then adding the results together to (4.4), and summing up the result from k = 0 to k = n - 1, we obtain

$$\begin{split} \varepsilon_{0}(\|\boldsymbol{E}_{h}^{n}\|_{\varepsilon_{\infty}}^{2} - \|\boldsymbol{E}_{h}^{0}\|_{\varepsilon_{\infty}}^{2}) + \varepsilon_{0} \sum_{q=0}^{Q} \left(\|\boldsymbol{J}_{qh}^{n+\frac{1}{2}}\|_{A_{q}}^{2} - \|\boldsymbol{J}_{qh}^{\frac{1}{2}}\|_{A_{q}}^{2} + \|\boldsymbol{P}_{qh}^{n}\|_{C_{q}}^{2} - \|\boldsymbol{P}_{qh}^{0}\|_{C_{q}}^{2} \right) \\ + \mu_{0}(\|\boldsymbol{H}_{h}^{n+\frac{1}{2}}\|_{\boldsymbol{\mu}_{\infty}}^{2} - \|\boldsymbol{H}_{h}^{\frac{1}{2}}\|_{\boldsymbol{\mu}_{\infty}}^{2}) + \mu_{0} \sum_{l=0}^{L} \left(\|\boldsymbol{K}_{lh}^{n}\|_{\tilde{A}_{l}}^{2} - \|\boldsymbol{K}_{lh}^{0}\|_{\tilde{A}_{l}}^{2} \right) \\ + \|\boldsymbol{M}_{lh}^{n+\frac{1}{2}}\|_{C_{l}}^{2} - \|\boldsymbol{M}_{lh}^{\frac{1}{2}}\|_{\tilde{C}_{l}}^{2} \right) \\ \leq \tau(\nabla \times \boldsymbol{E}_{h}^{0}, \boldsymbol{H}_{h}^{\frac{1}{2}}) + \tau\mu_{0} \sum_{l=0}^{L} \left[(\boldsymbol{K}_{lh}^{n}, \tilde{C}_{l} \boldsymbol{M}_{lh}^{n+\frac{1}{2}}) - (\boldsymbol{K}_{lh}^{0}, \tilde{C}_{l} \boldsymbol{M}_{lh}^{\frac{1}{2}}) \right. \\ + (\boldsymbol{g}_{l} \boldsymbol{K}_{lh}^{0}, \boldsymbol{H}_{h}^{\frac{1}{2}}) - (\boldsymbol{g}_{l} \boldsymbol{K}_{lh}^{n}, \boldsymbol{H}_{h}^{n+\frac{1}{2}}) \right] \\ - \tau(\nabla \times \boldsymbol{E}_{h}^{n}, \boldsymbol{H}_{h}^{n+\frac{1}{2}}) + \tau\varepsilon_{0} \sum_{q=0}^{Q} \left[(\boldsymbol{J}_{qh}^{\frac{1}{2}}, C_{q} \boldsymbol{P}_{qh}^{0}) - (\boldsymbol{J}_{qh}^{n+\frac{1}{2}}, C_{q} \boldsymbol{P}_{qh}^{n}) \right. \\ \left. + (\boldsymbol{f}_{q} \boldsymbol{J}_{qh}^{n+\frac{1}{2}}, \boldsymbol{E}_{h}^{n}) - (\boldsymbol{f}_{q} \boldsymbol{J}_{qh}^{\frac{1}{2}}, \boldsymbol{E}_{h}^{0}) \right]. \end{split}$$

Now we just need to estimate each term in (4.7). Using the inequality $(a,b) \le \delta \|a\|_0^2 + \frac{1}{4\delta} \|b\|_0^2$, the inverse estimate (4.1), and the CFL condition (4.2), we have

$$\tau(\boldsymbol{H}_{h}^{n+\frac{1}{2}}, \nabla \times \boldsymbol{E}_{h}^{n}) = (\sqrt{\mu_{0}}\boldsymbol{H}_{h}^{n+\frac{1}{2}}, \tau C_{v}\sqrt{\varepsilon_{0}}\nabla \times \boldsymbol{E}_{h}^{n}) \\
\leq \delta_{1}\mu_{0} \|\boldsymbol{H}_{h}^{n+\frac{1}{2}}\|_{0}^{2} + \frac{(\tau C_{v}C_{inv})^{2}}{4\delta_{1}h^{2}} \varepsilon_{0} \|\boldsymbol{E}_{h}^{n}\|_{0}^{2} \leq \delta_{1}\mu_{0} \|\boldsymbol{H}_{h}^{n+\frac{1}{2}}\|_{\boldsymbol{\mu}_{\infty}}^{2} + \frac{\varepsilon_{0}}{16\delta_{1}} \|\boldsymbol{E}_{h}^{n}\|_{\boldsymbol{\varepsilon}_{\infty}}^{2}, \\
(4.8b) \\
\tau(\boldsymbol{K}_{lh}^{n}, \tilde{C}_{l}\boldsymbol{M}_{lh}^{n+\frac{1}{2}}) \leq \delta_{2} \|\boldsymbol{M}_{lh}^{n+\frac{1}{2}}\|_{C_{l}}^{2} + \frac{\tau^{2}}{4\delta_{2}} \|\boldsymbol{K}_{lh}^{n}\|_{\tilde{C}_{l}}^{2} \leq \delta_{2} \|\boldsymbol{M}_{lh}^{n+\frac{1}{2}}\|_{C_{l}}^{2} + \frac{1}{16\delta_{2}} \|\boldsymbol{K}_{lh}^{n}\|_{L_{l}}^{2}, \\
(4.8c) \\
\tau(\boldsymbol{J}_{lh}^{n+\frac{1}{2}}, C_{q}\boldsymbol{P}_{qh}^{n}) \leq \delta_{3} \|\boldsymbol{P}_{qh}^{n}\|_{C_{q}}^{2} + \frac{\tau^{2}}{4\delta_{3}} \|\boldsymbol{J}_{qh}^{n+\frac{1}{2}}\|_{C_{q}}^{2} \leq \delta_{3} \|\boldsymbol{P}_{qh}^{n}\|_{C_{q}}^{2} + \frac{1}{16\delta_{3}} \|\boldsymbol{J}_{qh}^{n+\frac{1}{2}}\|_{A_{q}}^{2}, \\
(4.8d) \\
\tau(\boldsymbol{f}_{q}\boldsymbol{J}_{qh}^{n+\frac{1}{2}}, \boldsymbol{E}_{h}^{n}) = \tau(\boldsymbol{f}_{q}^{\frac{1}{2}}\boldsymbol{\omega}_{p}^{-1}\boldsymbol{J}_{qh}^{n+\frac{1}{2}}, \boldsymbol{f}_{q}^{\frac{1}{2}}\boldsymbol{\omega}_{p}\boldsymbol{E}_{h}^{n}) \leq \delta_{4} \|\boldsymbol{J}_{qh}^{n+\frac{1}{2}}\|_{A_{q}}^{2} + \frac{\tau^{2}}{4\delta_{4}} \|\boldsymbol{E}_{h}^{n}\|_{\boldsymbol{\varepsilon}_{\infty}}^{2}, \\
\leq \delta_{4} \|\boldsymbol{J}_{qh}^{n+\frac{1}{2}}\|_{A_{q}}^{2} + \frac{1}{16(Q+1)\delta_{4}} \|\boldsymbol{E}_{h}^{n}\|_{0}^{2} \leq \delta_{4} \|\boldsymbol{J}_{qh}^{n+\frac{1}{2}}\|_{A_{q}}^{2} + \frac{1}{16(Q+1)\delta_{4}} \|\boldsymbol{E}_{h}^{n}\|_{\boldsymbol{\varepsilon}_{\infty}}^{2}, \\
(4.8e) \\
\tau(\boldsymbol{g}_{l}\boldsymbol{K}_{lh}^{n}, \boldsymbol{H}_{h}^{n+\frac{1}{2}}) = \tau(\boldsymbol{g}_{l}^{\frac{1}{2}}\boldsymbol{\omega}_{m}^{-1}\boldsymbol{K}_{lh}^{n}, \boldsymbol{g}_{l}^{\frac{1}{2}}\boldsymbol{\omega}_{m}\boldsymbol{H}_{h}^{n+\frac{1}{2}}) \leq \delta_{5} \|\boldsymbol{K}_{lh}^{n}\|_{A_{l}}^{2} + \frac{\tau^{2}}{4\delta_{5}} \|\boldsymbol{H}_{h}^{n+\frac{1}{2}}\|_{\boldsymbol{g}_{l}\boldsymbol{\omega}_{m}}^{2}, \\
\leq \delta_{5} \|\boldsymbol{K}_{lh}^{n}\|_{A_{l}}^{2} + \frac{1}{16(L+1)\delta_{5}} \|\boldsymbol{H}_{h}^{n+\frac{1}{2}}\|_{0}^{2} \leq \delta_{5} \|\boldsymbol{K}_{lh}^{n}\|_{A_{l}}^{2} + \frac{1}{16(L+1)\delta_{5}} \|\boldsymbol{H}_{h}^{n+\frac{1}{2}}\|_{\boldsymbol{\mu}_{\infty}}^{2}.$$

Note that the above estimates hold true for n=0 too.

(III) Substituting all estimates (4.8) into (4.7), then combining like terms, and taking $\delta_1 = \delta_2 = \delta_3 = \delta_4 = \delta_5 = \frac{1}{4}$, we can reduce (4.7) to

$$\varepsilon_{0} \|\boldsymbol{E}_{h}^{n}\|_{\varepsilon_{\infty}}^{2} + \varepsilon_{0} \sum_{q=0}^{Q} \left(\|\boldsymbol{J}_{qh}^{n+\frac{1}{2}}\|_{A_{q}}^{2} + \frac{3}{2} \|\boldsymbol{P}_{qh}^{n}\|_{C_{q}}^{2} \right) + \mu_{0} \|\boldsymbol{H}_{h}^{n+\frac{1}{2}}\|_{\boldsymbol{\mu}_{\infty}}^{2}$$

$$+ \mu_{0} \sum_{l=0}^{L} \left(\|\boldsymbol{K}_{lh}^{n}\|_{\tilde{A}_{l}}^{2} + \frac{3}{2} \|\boldsymbol{M}_{lh}^{n+\frac{1}{2}}\|_{\tilde{C}_{l}}^{2} \right)$$

$$\leq 3\varepsilon_{0} \|\boldsymbol{E}_{h}^{0}\|_{\varepsilon_{\infty}}^{2} + \varepsilon_{0} \sum_{q=0}^{Q} \left(3 \|\boldsymbol{J}_{qh}^{\frac{1}{2}}\|_{A_{q}}^{2} + \frac{5}{2} \|\boldsymbol{P}_{qh}^{0}\|_{C_{q}}^{2} \right) + 3\mu_{0} \|\boldsymbol{H}_{h}^{\frac{1}{2}}\|_{\boldsymbol{\mu}_{\infty}}^{2}$$

$$+ \mu_{0} \sum_{l=0}^{L} \left(3 \|\boldsymbol{K}_{lh}^{0}\|_{\tilde{A}_{l}}^{2} + \frac{5}{2} \|\boldsymbol{M}_{lh}^{\frac{1}{2}}\|_{\tilde{C}_{l}}^{2} \right),$$

which concludes the proof of (4.3), since all the left-hand side coefficients of (4.9) are bounded below by 1, and all the right-hand side coefficients of (4.9) are bounded above by 3.

Remark 4.2. We would like to remark that when L = -1 (the common nonmagnetic case with $\mu_{\infty} = I_3 := \text{diag}(1,1,1)$), the CFL condition (4.2) reduces to

and the stability (4.3) reduces to

$$(4.11) \qquad \varepsilon_{0} \|\boldsymbol{E}_{h}^{n}\|_{\boldsymbol{\varepsilon}_{\infty}}^{2} + \varepsilon_{0} \sum_{q=0}^{Q} \left(\|\boldsymbol{J}_{qh}^{n+\frac{1}{2}}\|_{A_{q}}^{2} + \|\boldsymbol{P}_{qh}^{n}\|_{C_{q}}^{2} \right) + \mu_{0} \|\boldsymbol{H}_{h}^{n+\frac{1}{2}}\|_{\boldsymbol{\mu}_{\infty}}^{2}$$

$$\leq 3 \left[\varepsilon_{0} \|\boldsymbol{E}_{h}^{0}\|_{\boldsymbol{\varepsilon}_{\infty}}^{2} + \varepsilon_{0} \sum_{q=0}^{Q} \left(\|\boldsymbol{J}_{qh}^{\frac{1}{2}}\|_{A_{q}}^{2} + \|\boldsymbol{P}_{qh}^{0}\|_{C_{q}}^{2} \right) + \mu_{0} \|\boldsymbol{H}_{h}^{\frac{1}{2}}\|_{\boldsymbol{\mu}_{\infty}}^{2} \right].$$

Another special case is Q = L = -1 with $\varepsilon_{\infty} = \mu_{\infty} = I_3$, which corresponds to the free space case. In this case, the CFL condition (4.2) reduces to

and the stability (4.3) reduces to

5. The optimal error estimate. To make the error analysis easy to follow, we denote the solution errors by the corresponding curly letters,

$${\mathscr E}_h^n = {m E}_h^n - {m E}(\cdot,t_n), \;\; {\mathscr H}_h^{n+rac{1}{2}} = {m H}_h^{n+rac{1}{2}} - {m H}(\cdot,t_{n+rac{1}{2}}), \;\; {\mathscr J}_{qh}^{n+rac{1}{2}} = {m J}_{qh}^{n+rac{1}{2}} - {m J}_q(\cdot,t_{n+rac{1}{2}}), \ {\mathscr P}_{qh}^n = {m P}_{qh}^n - {m P}_q(\cdot,t_n), \;\; {\mathscr H}_{lh}^n = {m K}_{lh}^n - {m K}_l(\cdot,t_n), \;\; {\mathscr M}_{lh}^{n+rac{1}{2}} = {m M}_{lh}^{n+rac{1}{2}} - {m M}_l(\cdot,t_{n+rac{1}{2}}), \ {\mathcal P}_{qh}^n = {m P}_{qh}^n - {m P}_q(\cdot,t_n), \;\; {\mathscr H}_{lh}^n = {m K}_{lh}^n - {m K}_l(\cdot,t_n), \;\; {\mathscr H}_{lh}^{n+rac{1}{2}} = {m M}_{lh}^{n+rac{1}{2}} - {m M}_l(\cdot,t_{n+rac{1}{2}}), \ {\mathcal P}_{qh}^n = {m P}_{qh}^n - {m P}_q(\cdot,t_n), \;\; {\mathcal H}_{lh}^n = {m K}_{lh}^n - {m K}_l(\cdot,t_n), \;\; {\mathcal H}_{lh}^{n+rac{1}{2}} = {m M}_{lh}^{n+rac{1}{2}} - {m M}_l(\cdot,t_{n+rac{1}{2}}), \ {\mathcal H}_{lh}^n = {m H}_{lh}^n - {m H}_{lh$$

and some intermediate errors given as follows:

$$egin{aligned} oldsymbol{\mathcal{E}}_I = r_h E - E, \ oldsymbol{\mathcal{J}}_{qI} = r_h oldsymbol{J}_q - oldsymbol{J}_q, & oldsymbol{\mathcal{P}}_{qI} = r_h oldsymbol{P}_q - oldsymbol{P}_q, \ oldsymbol{\mathcal{H}}_I = oldsymbol{w}_h oldsymbol{H} - oldsymbol{H}_l, & oldsymbol{\mathcal{M}}_{lI} = oldsymbol{w}_h oldsymbol{M}_l - oldsymbol{M}_l, \ oldsymbol{\mathcal{E}}_h = r_h E - E_h, \ oldsymbol{\mathcal{J}}_{qh} = r_h oldsymbol{J}_q - oldsymbol{J}_{qh}, & oldsymbol{\mathcal{P}}_{qh} = r_h oldsymbol{P}_q - oldsymbol{P}_{qh}, \ oldsymbol{\mathcal{H}}_h = oldsymbol{w}_h oldsymbol{H} - oldsymbol{H}_h, \ oldsymbol{\mathcal{M}}_{lh} = oldsymbol{w}_h oldsymbol{M}_l - oldsymbol{M}_{lh}. \end{aligned}$$

To establish the following optimal error estimate for scheme (3.1), we denote the time intervals $I_k = [t_k, t_{k+1}]$ and $I'_k = [t_{k+\frac{1}{2}}, t_{k+\frac{3}{2}}]$.

Theorem 5.1. Suppose that the solution of (2.8) satisfies the following regularity assumptions:

$$\begin{split} \boldsymbol{E}, \boldsymbol{J}_q, \boldsymbol{P}_q \in L^{\infty}(0, T; H^{\alpha}(curl; \Omega)), \quad \boldsymbol{H}, \boldsymbol{K}_l, \boldsymbol{M}_l \in L^{\infty}(0, T; (L^2(\Omega))^3), \\ \partial_t \boldsymbol{E}, \partial_t \boldsymbol{J}_q, \partial_t \boldsymbol{P}_q \in L^2(0, T; H^{\alpha}(curl; \Omega)), \\ \nabla \times \partial_{tt} \boldsymbol{E}, \partial_{tt} \boldsymbol{E}, \nabla \times \partial_{tt} \boldsymbol{H}, \partial_{tt} \boldsymbol{H}, \partial_{tt} \boldsymbol{J}_q, \partial_{tt} \boldsymbol{P}_q, \partial_{tt} \boldsymbol{K}_l, \partial_{tt} \boldsymbol{M}_l \in L^2(0, T; (L^2(\Omega))^3) \end{split}$$

 $\mathbf{V} \times O_{tt}\mathbf{E}, O_{tt}\mathbf{E}, \mathbf{V} \times O_{tt}\mathbf{H}, O_{tt}\mathbf{H}, O_{tt}\mathbf{H}, O_{tt}\mathbf{F}_q, O_{tt}\mathbf{K}_l, O_{tt}\mathbf{M}_l \in L \ (0, 1, (L \ (2l)) \)$

with $\frac{1}{2} < \alpha \le 1$. If the time step $\tau \le 1$ satisfies (4.2) and the scheme (3.1) adopts the initial approximations (3.2a)–(3.2c), then we have the optimal error estimate:

(5.1)
$$\mu_{0} \| \mathcal{H}_{h}^{n+\frac{1}{2}} \|_{\boldsymbol{\mu}_{\infty}}^{2} + \mu_{0} \sum_{l=0}^{L} (\| \mathcal{K}_{lh}^{n} \|_{\tilde{A}_{l}}^{2} + \| \mathcal{M}_{lh}^{n+\frac{1}{2}} \|_{\tilde{C}_{l}}^{2}) + \varepsilon_{0} \| \mathcal{E}_{h}^{n} \|_{\boldsymbol{\varepsilon}_{\infty}}^{2} + \varepsilon_{0} \sum_{q=0}^{Q} (\| \mathcal{J}_{qh}^{n+\frac{1}{2}} \|_{A_{q}}^{2} + \| \mathcal{P}_{qh}^{n} \|_{C_{q}}^{2}) \leq C(h^{\alpha} + \tau^{2})^{2},$$

where the constant C > 0 is independent of τ and h.

Proof. Integrating (2.8a), (2.8c), and (2.8e) from t_k to t_{k+1} , and (2.8b), (2.8d), and (2.8f) from $t_{k+\frac{1}{2}}$ to $t_{k+\frac{3}{2}}$, then multiplying the respective results by $\frac{\psi_h}{\tau}$, $\frac{\tilde{\psi}_{qh}}{\tau}$, $\frac{\varphi_{lh}}{\tau}$, $\frac{\varphi_{qh}}{\tau}$, $\frac{\varphi_{h}}{\tau}$, $\frac{\varphi_{h}}{\tau}$, integrating over Ω , and subtracting the corresponding results from those in (3.1), we obtain

$$\varepsilon_{0}(\varepsilon_{\infty}\delta_{\tau}\mathcal{E}_{h}^{k+\frac{1}{2}},\psi_{h}) - (\mathcal{H}_{h}^{k+\frac{1}{2}},\nabla\times\psi_{h}) + \varepsilon_{0}\sum_{q=0}^{Q}(f_{q}\mathcal{J}_{qh}^{k+\frac{1}{2}},\psi_{h}) \\
= \varepsilon_{0}(\varepsilon_{\infty}\delta_{\tau}\mathcal{E}_{I}^{k+\frac{1}{2}},\psi_{h}) - \left(w_{h}H^{k+\frac{1}{2}} - \frac{1}{\tau}\int_{I_{k}}H,\nabla\times\psi_{h}\right) \\
+ \varepsilon_{0}\sum_{q=0}^{Q}\left(f_{q}\left(r_{h}\mathcal{J}_{q}^{k+\frac{1}{2}} - \frac{1}{\tau}\int_{I_{k}}J_{q}\right),\psi_{h}\right), \\
(5.2b) \\
(\delta_{\tau}\mathcal{K}_{lh}^{k+\frac{1}{2}},\varphi_{lh}) + (\Gamma_{ml}\overline{\mathcal{K}}_{lh}^{k+\frac{1}{2}},\varphi_{lh}) - (\omega_{m}^{2}\mathcal{H}_{h}^{k+\frac{1}{2}},\varphi_{lh}) + (\omega_{ml}^{2}\mathcal{M}_{lh}^{k+\frac{1}{2}},\varphi_{lh}) \\
= \left(\Gamma_{ml}\left(w_{h}\overline{\mathcal{K}}_{l}^{k+\frac{1}{2}} - \frac{1}{\tau}\int_{I_{k}}K_{l}\right),\varphi_{lh}\right) + (\delta_{\tau}\mathcal{K}_{lI}^{k+\frac{1}{2}},\varphi_{lh}) \\
- \left(\omega_{m}^{2}\left(w_{h}H^{k+\frac{1}{2}} - \frac{1}{\tau}\int_{I_{k}}H\right),\varphi_{lh}\right) + \left(\omega_{ml}^{2}\left(w_{h}M_{l}^{k+\frac{1}{2}} - \frac{1}{\tau}\int_{I_{k}}M_{l}\right),\varphi_{lh}\right), \\
(5.2c) \\
\mu_{0}(\mu_{\infty}\delta_{\tau}\mathcal{H}_{h}^{k+1},\varphi_{h}) + (\nabla\times\mathcal{E}_{h}^{k+1},\varphi_{h}) + \mu_{0}\sum_{l=0}^{L}(g_{l}\mathcal{K}_{lh}^{k+1},\varphi_{h}) \\
= \mu_{0}(\mu_{\infty}\delta_{\tau}\mathcal{H}_{l}^{k+1},\varphi_{h}) + \left(\nabla\times r_{h}E^{k+1} - \frac{1}{\tau}\int_{I_{k}'}\nabla\times E,\varphi_{h}\right) \\
+ \mu_{0}\sum_{l=0}^{L}\left(g_{l}(w_{h}K_{l}^{k+1} - \frac{1}{\tau}\int_{I_{k}'}K_{l}),\varphi_{h}\right), \\$$

(5.2d)

$$(A_{q}\boldsymbol{\Gamma}_{eq}\overline{\boldsymbol{\mathcal{J}}}_{qh}^{k+1},\boldsymbol{\psi}_{qh}) + (A_{q}\delta_{\tau}\boldsymbol{\mathcal{J}}_{qh}^{k+1},\boldsymbol{\psi}_{qh}) - (\boldsymbol{f}_{q}\boldsymbol{\mathcal{E}}_{h}^{k+1},\boldsymbol{\psi}_{qh}) + (C_{q}\boldsymbol{\mathcal{P}}_{qh}^{k+1},\boldsymbol{\psi}_{qh})$$

$$= (A_{q}\delta_{\tau}\boldsymbol{\mathcal{J}}_{qI}^{k+1},\boldsymbol{\psi}_{qh}) + \left(A_{q}\boldsymbol{\Gamma}_{eq}\left(\boldsymbol{r}_{h}\overline{\boldsymbol{\mathcal{J}}}_{q}^{k+1} - \frac{1}{\tau}\int_{I_{k}'}\boldsymbol{J}_{q}\right),\boldsymbol{\psi}_{qh}\right)$$

$$- \left(\boldsymbol{f}_{q}\left(\boldsymbol{r}_{h}\boldsymbol{E}^{k+1} - \frac{1}{\tau}\int_{I_{k}'}\boldsymbol{E}\right),\boldsymbol{\psi}_{qh}\right) + \left(C_{q}\left(\boldsymbol{r}_{h}\boldsymbol{P}_{q}^{k+1} - \frac{1}{\tau}\int_{I_{k}'}\boldsymbol{P}_{q}\right),\boldsymbol{\psi}_{qh}\right),$$

$$(5.2e)$$

$$(\delta_{\tau}\boldsymbol{\mathcal{P}}_{qh}^{k+\frac{1}{2}},\tilde{\boldsymbol{\psi}}_{qh}) - (\boldsymbol{\mathcal{J}}_{qh}^{k+\frac{1}{2}},\tilde{\boldsymbol{\psi}}_{qh}) = (\delta_{\tau}\boldsymbol{\mathcal{P}}_{qI}^{k+\frac{1}{2}},\tilde{\boldsymbol{\psi}}_{qh}) - \left(\boldsymbol{r}_{h}\boldsymbol{J}_{q}^{k+\frac{1}{2}} - \frac{1}{\tau}\int_{I_{k}}\boldsymbol{J}_{q},\tilde{\boldsymbol{\psi}}_{qh}\right),$$

$$(5.2f)$$

$$(\delta_{\tau}\boldsymbol{\mathcal{M}}_{lh}^{k+1},\tilde{\boldsymbol{\varphi}}_{lh}) - (\boldsymbol{\mathcal{K}}_{lh}^{k+1},\tilde{\boldsymbol{\varphi}}_{lh}) = (\delta_{\tau}\boldsymbol{\mathcal{M}}_{lI}^{k+1},\tilde{\boldsymbol{\varphi}}_{lh}) - \left(\boldsymbol{w}_{h}\boldsymbol{K}_{l}^{k+1} - \frac{1}{\tau}\int_{I_{k}'}\boldsymbol{K}_{l},\tilde{\boldsymbol{\varphi}}_{lh}\right).$$

Taking $\varphi_h = 2\tau \overline{\mathcal{H}}_h^{k+1}$, $\psi_h = 2\tau \overline{\mathcal{E}}_h^{k+\frac{1}{2}}$, $\psi_{qh} = 2\varepsilon_0\tau \overline{\mathcal{J}}_{qh}^{k+1}$, $\tilde{\psi}_{qh} = 2\varepsilon_0\tau \Pi_{qh} \overline{\mathcal{P}}_{qh}^{k+\frac{1}{2}}$, $\varphi_{lh} = 2\mu_0\tau \tilde{A}_l \overline{\mathcal{K}}_{lh}^{k+\frac{1}{2}}$, $\tilde{\varphi}_{lh} = 2\mu_0\tau \tilde{C}_l \overline{\mathcal{M}}_{lh}^{k+1}$ in (5.2), then adding the results together, and summing up from k=0 to k=n-1, we obtain

$$\begin{split} &(5.3)\\ &\varepsilon_{0}(\|\mathcal{E}_{h}^{n}\|_{\varepsilon_{\infty}}^{2} - \|\mathcal{E}_{h}^{0}\|_{\varepsilon_{\infty}}^{2}) + \varepsilon_{0} \sum_{q=0}^{Q} (\|\mathcal{J}_{qh}^{n+\frac{1}{2}}\|_{A_{q}}^{2} - \|\mathcal{J}_{qh}^{\frac{1}{2}}\|_{A_{q}}^{2} + \|\mathcal{P}_{qh}^{n}\|_{C_{q}}^{2} - \|\mathcal{P}_{qh}^{0}\|_{C_{q}}^{2}) \\ &+ \mu_{0}(\|\mathcal{H}_{h}^{n+\frac{1}{2}}\|_{\mu_{\infty}}^{2} - \|\mathcal{H}_{h}^{\frac{1}{2}}\|_{\mu_{\infty}}^{2}) + \mu_{0} \sum_{l=0}^{L} (\|\mathcal{K}_{lh}^{n}\|_{\tilde{A}_{l}}^{2} - \|\mathcal{K}_{lh}^{0}\|_{\tilde{A}_{l}}^{2} + \|\mathcal{M}_{lh}^{n+\frac{1}{2}}\|_{\tilde{C}_{l}}^{2} - \|\mathcal{M}_{lh}^{\frac{1}{2}}\|_{\tilde{C}_{l}}^{2}) \\ &\leq \tau(\mathcal{H}_{h}^{\frac{1}{2}}, \nabla \times \mathcal{E}_{h}^{0}) + \tau\mu_{0} \sum_{l=0}^{L} \left[(g_{l}\mathcal{K}_{lh}^{0}, \mathcal{H}_{h}^{\frac{1}{2}}) - (g_{l}\mathcal{K}_{lh}^{n}, \mathcal{H}_{h}^{n+\frac{1}{2}}) + (\mathcal{M}_{lh}^{n+\frac{1}{2}}, \tilde{C}_{l}\mathcal{K}_{lh}^{n}) - (\mathcal{M}_{lh}^{\frac{1}{2}}, \tilde{C}_{l}\mathcal{K}_{lh}^{0}) \right] \\ &- \tau(\mathcal{H}_{h}^{n+\frac{1}{2}}, \nabla \times \mathcal{E}_{h}^{0}) + \tau\varepsilon_{0} \sum_{q=0}^{Q} \left[(f_{q}\mathcal{J}_{qh}^{n+\frac{1}{2}}, \mathcal{E}_{h}^{n}) - (f_{q}\mathcal{J}_{qh}^{\frac{1}{2}}, \mathcal{E}_{h}^{0}) + (\mathcal{P}_{qh}^{0}, C_{q}\mathcal{J}_{qh}^{\frac{1}{2}}) - (\mathcal{P}_{qh}^{n}, C_{q}\mathcal{J}_{qh}^{\frac{1}{2}}) \right] \\ &+ 2\tau\varepsilon_{0} \sum_{k=0}^{n-1} (\varepsilon_{\infty}\delta_{\tau}\mathcal{E}_{l}^{k+\frac{1}{2}}, \overline{\mathcal{E}}_{h}^{k+\frac{1}{2}}) - 2\tau \sum_{k=0}^{n-1} \left(w_{h}H^{k+\frac{1}{2}} - \frac{1}{\tau} \int_{I_{k}} H, \nabla \times \overline{\mathcal{E}}_{h}^{k+\frac{1}{2}} \right) \\ &+ 2\tau\mu_{0} \sum_{k=0}^{n-1} (\mu_{\infty}\delta_{\tau}\mathcal{H}_{l}^{k+1}, \overline{\mathcal{H}}_{h}^{k+1}) + 2\tau \sum_{k=0}^{n-1} \left(\nabla \times r_{h}E^{k+1} - \frac{1}{\tau} \int_{I_{k}} \nabla \times E, \overline{\mathcal{H}}_{h}^{k+1} \right) \\ &+ 2\tau\varepsilon_{0} \sum_{q=0}^{N} \sum_{k=0}^{n-1} \left(f_{q}(r_{h}J_{q}^{k+\frac{1}{2}} - \frac{1}{\tau} \int_{I_{k}} J_{q}), \overline{\mathcal{F}}_{h}^{k+\frac{1}{2}} \right) \\ &+ 2\tau\varepsilon_{0} \sum_{q=0}^{N} \sum_{k=0}^{n-1} \left(A_{q}\Gamma_{eq} \left(r_{h}\overline{J}_{q}^{k+1} - \frac{1}{\tau} \int_{I_{k}} J_{q} \right), \overline{\mathcal{J}}_{qh}^{k+1} \right) + (A_{q}\delta_{\tau}\mathcal{J}_{qI}^{k+1}, \overline{\mathcal{J}}_{qh}^{k+1}) \\ &- \left(r_{h}E^{k+1} - \frac{1}{\tau} \int_{I_{k}} E, f_{q}\overline{\mathcal{J}}_{qh}^{k+1} \right) + \left(C_{q}(r_{h}P_{q}^{k+1} - \frac{1}{\tau} \int_{I_{k}} P_{q} \right), \overline{\mathcal{J}}_{qh}^{k+1}) \\ &+ (\delta_{\tau}P_{qI}^{k+\frac{1}{2}}, C_{q}\overline{\mathcal{P}}_{qh}^{k+\frac{1}{2}}) - \left(r_{h}J_{q}^{k+\frac{1}{2}} - \frac{1}{\tau} \int_{I_{k}} K_{l}), \overline{\mathcal{H}}_{h}^{k+1} \right) \right] \\ &+ 2\tau\mu_{0} \sum_{l=0}^{L} \sum_{k=0}^{N} \left(g_{l}(w_{h}K_{l}^{k+1} - \frac{1}{\tau} \int_{I_{k}} K_{l}), \overline{\mathcal{H}}_{h}^{k+1} \right) \right) \right]$$

$$\begin{split} &+2\tau\mu_0\sum_{l=0}^{L}\sum_{k=0}^{n-1}\left[\left(\mathbf{\Gamma}_{ml}\left(\mathbf{w}_h\overline{\mathbf{K}}_l^{k+\frac{1}{2}}-\frac{1}{\tau}\int_{I_k}\mathbf{K}_l\right),\tilde{A}_l\overline{\mathbf{K}}_{lh}^{k+\frac{1}{2}}\right)+\left(\delta_{\tau}\mathbf{K}_{lI}^{k+\frac{1}{2}},\tilde{A}_l\overline{\mathbf{K}}_{lh}^{k+\frac{1}{2}}\right)\right.\\ &-\left(\mathbf{w}_h\mathbf{H}^{k+\frac{1}{2}}-\frac{1}{\tau}\int_{I_k}\mathbf{H},\mathbf{g}_l\overline{\mathbf{K}}_{lh}^{k+\frac{1}{2}}\right)+\left(\boldsymbol{\omega}_{ml}^2\left(\mathbf{w}_h\mathbf{M}_l^{k+\frac{1}{2}}-\frac{1}{\tau}\int_{I_k}\mathbf{M}_l\right),\tilde{A}_l\overline{\mathbf{K}}_{lh}^{k+\frac{1}{2}}\right)\\ &+\left(\delta_{\tau}\mathbf{\mathcal{M}}_{lI}^{k+1},\tilde{C}_l\overline{\mathbf{\mathcal{M}}}_{lh}^{k+1}\right)-\left(\mathbf{w}_h\mathbf{K}_l^{k+1}-\frac{1}{\tau}\int_{I_k'}\mathbf{K}_l,\tilde{C}_l\overline{\mathbf{\mathcal{M}}}_{lh}^{k+1}\right)\right]\\ &=Err_1+\sum_{i=2}^{5}\sum_{l=0}^{L}Err_{i,l}+Err_6+\sum_{i=7}^{10}\sum_{q=0}^{Q}Err_{i,q}+\sum_{i=11}^{14}Err_i+\sum_{i=15}^{21}\sum_{q=0}^{Q}Err_{i,q}+\sum_{i=22}^{28}\sum_{l=0}^{L}Err_{i,l}. \end{split}$$

Now we need to estimate each term on the right-hand side of (5.3). The first ten terms can be estimated in the same way as (4.8), and the rest can be estimated by using the inequality $(a,b) \leq \delta \|a\|^2 + \frac{1}{4\delta} \|b\|^2$, the standard $(L^2(\Omega))^3$ projection error, the Nédélec interpolation error estimate [29, Theorem 5.41], and [22, Lemma 3.19]. Due to page limits, we skip the details. Then by the discrete Gronwall inequality, we have

$$\varepsilon_{0} \| \mathcal{E}_{h}^{n} \|_{\varepsilon_{\infty}}^{2} + \varepsilon_{0} \sum_{q=0}^{Q} (\| \mathcal{J}_{qh}^{n+\frac{1}{2}} \|_{A_{q}}^{2} + \| \mathcal{P}_{qh}^{n} \|_{C_{q}}^{2}) + \mu_{0} \| \mathcal{H}_{h}^{n+\frac{1}{2}} \|_{\boldsymbol{\mu}_{\infty}}^{2}
+ \mu_{0} \sum_{l=0}^{L} (\| \mathcal{K}_{lh}^{n} \|_{\tilde{A}_{l}}^{2} + \| \mathcal{M}_{lh}^{n+\frac{1}{2}} \|_{\tilde{C}_{l}}^{2}),
(5.4)$$

$$\leq C \left[\mu_{0} \| \mathcal{H}_{h}^{\frac{1}{2}} \|_{\boldsymbol{\mu}_{\infty}}^{2} + \varepsilon_{0} \| \mathcal{E}_{h}^{0} \|_{\boldsymbol{\varepsilon}_{\infty}}^{2} + \mu_{0} \sum_{l=0}^{L} \left(\| \mathcal{M}_{lh}^{\frac{1}{2}} \|_{\tilde{C}_{l}}^{2} + \| \mathcal{K}_{lh}^{0} \|_{\tilde{A}_{l}}^{2} \right) \right.
+ \varepsilon_{0} \sum_{q=0}^{Q} \left(\| \mathcal{J}_{qh}^{\frac{1}{2}} \|_{A_{q}}^{2} + \| \mathcal{P}_{qh}^{0} \|_{C_{q}}^{2} \right) \right] + C(h^{2\alpha} + \tau^{4}).$$

Finally, by the triangle inequality, the Nédélec interpolation, and L^2 projection error estimates, we conclude the proof.

6. Coupling with the anisotropic perfectly matched layer. To effectively simulate the wave propagation in an unbounded domain, we truncate the unbounded domain to a bounded one and use a perfectly matched layer (PML) to surround the truncated domain. Here we adopt an APML [13], which in the frequency domain is given as

(6.1)
$$j\omega\Lambda\widehat{D} = \nabla \times \widehat{H}, \ j\omega\Lambda\widehat{B} = -\nabla \times \widehat{E},$$

where the anisotropic medium tensor Λ is

$$\mathbf{\Lambda} = \operatorname{diag}(s_x^{-1} s_y s_z, s_x s_y^{-1} s_z, s_x s_y s_z^{-1}), \quad s_i = \kappa_i + \frac{\sigma_i}{j\omega\varepsilon_0}, \qquad i = x, y, z.$$

Moreover, the coefficients κ_i and damping functions σ_i are chosen as

$$\kappa_i = 1 + (\kappa_{max} - 1) \left(\frac{d_i}{d}\right)^m, \ \ \sigma_i = \sigma_{max} \left(\frac{d_i}{d}\right)^m,$$

with m=4, and $\sigma_{max}=-\frac{(m+1)\log(R_0)}{2d\sqrt{\mu_0/\varepsilon_0}}$, where d_i denotes the distance from the point \boldsymbol{x} in the PML region to the interface in the i direction, d denotes the PML thickness, and $R_0=10^{-8}$ denotes the reflectivity at the truncated boundary interface.

Denote $\Lambda_x = \operatorname{diag}(s_x, s_y, s_z)$, $\Lambda_y = \operatorname{diag}(s_y, s_z, s_x)$, and $\Lambda_z = \operatorname{diag}(s_z, s_x, s_y)$. We can rewrite Λ as $\Lambda = \Lambda_x^{-1} \Lambda_y \Lambda_z$. Introducing two new variables

(6.2)
$$\tilde{\boldsymbol{D}}(\omega) = \boldsymbol{\Lambda}_x^{-1} \boldsymbol{\Lambda}_z \hat{\boldsymbol{D}}(\omega), \ \tilde{\boldsymbol{B}}(\omega) = \boldsymbol{\Lambda}_x^{-1} \boldsymbol{\Lambda}_z \hat{\boldsymbol{B}}(\omega),$$

then applying the Fourier inverse transform to (6.1), (6.2), and

$$j\omega\widehat{\boldsymbol{B}} = j\omega\mu_0\boldsymbol{\mu}_{\infty}\widehat{\boldsymbol{H}} + \mu_0\sum_{l=0}^{L}\boldsymbol{g}_{l}\widehat{\boldsymbol{K}}_{l},\; j\omega\widehat{\boldsymbol{D}} = j\omega\mu_0\boldsymbol{\varepsilon}_{\infty}\widehat{\boldsymbol{E}} + \varepsilon_0\sum_{q=0}^{Q}\boldsymbol{f}_{q}\widehat{\boldsymbol{J}}_{q},$$

we obtain the time-domain APML governing equations given as

$$\begin{split} \mathcal{K}_2\partial_t \tilde{\boldsymbol{D}} + \varepsilon_0^{-1} \mathcal{Q}_2 \tilde{\boldsymbol{D}} &= \nabla \times \boldsymbol{H}, & \mathcal{K}_2\partial_t \tilde{\boldsymbol{B}} + \varepsilon_0^{-1} \mathcal{Q}_2 \tilde{\boldsymbol{B}} = -\nabla \times \boldsymbol{E}, \\ \mathcal{K}_1\partial_t \tilde{\boldsymbol{D}} + \varepsilon_0^{-1} \mathcal{Q}_1 \tilde{\boldsymbol{D}} &= \boldsymbol{K}_3\partial_t \boldsymbol{D} + \varepsilon_0^{-1} \mathcal{Q}_3 \boldsymbol{D}, & \mathcal{K}_1\partial_t \tilde{\boldsymbol{B}} + \varepsilon_0^{-1} \mathcal{Q}_1 \tilde{\boldsymbol{B}} = \boldsymbol{K}_3\partial_t \boldsymbol{B} + \varepsilon_0^{-1} \mathcal{Q}_3 \boldsymbol{B}, \\ \varepsilon_0 \boldsymbol{\varepsilon}_\infty \partial_t \boldsymbol{E} + \varepsilon_0 \sum_{q=0}^Q \boldsymbol{f}_q \boldsymbol{J}_q &= \partial_t \boldsymbol{D}, & \mu_0 \boldsymbol{\mu}_\infty \partial_t \boldsymbol{H} + \mu_0 \sum_{l=0}^L \boldsymbol{g}_l \boldsymbol{K}_l &= \partial_t \boldsymbol{B}, \\ \partial_t \boldsymbol{P}_q &= \boldsymbol{J}_q, & \partial_t \boldsymbol{M}_l &= \boldsymbol{K}_l, \\ \partial_t \boldsymbol{J}_q + \boldsymbol{\Gamma}_{eq} \boldsymbol{J}_q &= \boldsymbol{\omega}_p^2 \boldsymbol{E} - \boldsymbol{\omega}_{eq}^2 \boldsymbol{P}_q, & \partial_t \boldsymbol{K}_l + \boldsymbol{\Gamma}_{ml} \boldsymbol{K}_l &= \boldsymbol{\omega}_m^2 \boldsymbol{H} - \boldsymbol{\omega}_{ml}^2 \boldsymbol{M}_l, \end{split}$$

where we denote matrices $\mathcal{K}_1 = \operatorname{diag}(\kappa_x, \kappa_y, \kappa_z)$, $\mathcal{K}_2 = \operatorname{diag}(\kappa_y, \kappa_z, \kappa_x)$, $\mathcal{K}_3 = \operatorname{diag}(\kappa_z, \kappa_x, \kappa_y)$, $\mathcal{Q}_1 = \operatorname{diag}(\sigma_x, \sigma_y, \sigma_z)$, $\mathcal{Q}_2 = \operatorname{diag}(\sigma_y, \sigma_z, \sigma_x)$, $\mathcal{Q}_3 = \operatorname{diag}(\sigma_z, \sigma_x, \sigma_y)$, $q = 0, 1, \ldots, Q$, and $l = 0, 1, \ldots, L$.

We propose the following leapfrog scheme to solve the above APML model with a PEC boundary condition: Given proper initial approximations $\boldsymbol{E}_h^0, \boldsymbol{D}_h^0, \tilde{\boldsymbol{D}}_h^0, \boldsymbol{H}_h^{\frac{1}{2}}, \tilde{\boldsymbol{B}}_h^{\frac{1}{2}}, \boldsymbol{B}_h^{\frac{1}{2}}, \boldsymbol{J}_{qh}^{\frac{1}{2}}, \boldsymbol{P}_{qh}^0, \boldsymbol{M}_{lh}^{\frac{1}{2}}$ and \boldsymbol{K}_{lh}^0 , find $\boldsymbol{E}_h^{k+1}, \tilde{\boldsymbol{D}}_h^{k+1}, \boldsymbol{D}_h^{k+1} \in \boldsymbol{V}_h^0, \boldsymbol{J}_{qh}^{k+\frac{3}{2}}, \boldsymbol{P}_{qh}^{k+1} \in \boldsymbol{V}_h, \boldsymbol{H}_h^{k+\frac{3}{2}}, \tilde{\boldsymbol{B}}_h^{k+\frac{3}{2}}, \boldsymbol{B}_h^{k+\frac{3}{2}}, \boldsymbol{K}_{lh}^{k+1}, \boldsymbol{M}_{lh}^{k+\frac{3}{2}} \in \boldsymbol{U}_h$, such that

$$(6.3\mathrm{a}) \qquad (\mathcal{K}_2 \delta_\tau \tilde{\boldsymbol{D}}_h^{k+\frac{1}{2}}, \boldsymbol{\psi}_h) + \varepsilon_0^{-1} (\boldsymbol{\mathcal{Q}}_2 \overline{\tilde{\boldsymbol{D}}}_h^{k+\frac{1}{2}}, \boldsymbol{\psi}_h) = (\boldsymbol{H}_h^{k+\frac{1}{2}}, \nabla \times \boldsymbol{\psi}_h),$$

(6.3b)
$$(\mathcal{K}_{3}\delta_{\tau}\boldsymbol{D}_{h}^{k+\frac{1}{2}},\tilde{\boldsymbol{\psi}}_{h}) + \varepsilon_{0}^{-1}(\boldsymbol{Q}_{3}\overline{\boldsymbol{D}}_{h}^{k+\frac{1}{2}},\tilde{\boldsymbol{\psi}}_{h}) = (\mathcal{K}_{1}\delta_{\tau}\tilde{\boldsymbol{D}}_{h}^{k+\frac{1}{2}},\tilde{\boldsymbol{\psi}}_{h}) + \varepsilon_{0}^{-1}(\boldsymbol{Q}_{1}\overline{\tilde{\boldsymbol{D}}}_{h}^{k+\frac{1}{2}},\tilde{\boldsymbol{\psi}}_{h}),$$

(6.3c)
$$(\delta_{\tau} \boldsymbol{P}_{qh}^{k+\frac{1}{2}}, \tilde{\boldsymbol{\psi}}_{qh}) = (\boldsymbol{J}_{qh}^{k+\frac{1}{2}}, \tilde{\boldsymbol{\psi}}_{qh}),$$

(6.3d)
$$(\delta_{\tau} \boldsymbol{J}_{qh}^{k+1}, \boldsymbol{\psi}_{qh}) + (\Gamma_{eq} \overline{\boldsymbol{J}}_{qh}^{k+1}, \boldsymbol{\psi}_{qh}) = (\boldsymbol{\omega}_{p}^{2} \boldsymbol{E}_{h}^{k+1}, \boldsymbol{\psi}_{qh}) - (\boldsymbol{\omega}_{eq}^{2} \boldsymbol{P}_{qh}^{k+1}, \boldsymbol{\psi}_{qh}),$$

(6.3e)
$$\varepsilon_0(\boldsymbol{\varepsilon}_{\infty}\delta_{\tau}\boldsymbol{E}_h^{k+\frac{1}{2}}, \hat{\boldsymbol{\psi}}_h) + \varepsilon_0 \sum_{q=0}^{Q} (\boldsymbol{f}_{\boldsymbol{q}}\boldsymbol{J}_{qh}^{k+\frac{1}{2}}, \hat{\boldsymbol{\psi}}_h) = (\delta_{\tau}\boldsymbol{D}_h^{k+\frac{1}{2}}, \hat{\boldsymbol{\psi}}_h),$$

$$(6.3f) \qquad (\mathcal{K}_2 \delta_\tau \tilde{\boldsymbol{B}}_h^{k+1}, \boldsymbol{\varphi}_h) - \varepsilon_0^{-1} (\boldsymbol{\mathcal{Q}}_2 \overline{\tilde{\boldsymbol{B}}}_h^{k+1}, \boldsymbol{\varphi}_h) = -(\nabla \times \boldsymbol{E}_h^{k+1}, \boldsymbol{\varphi}_h),$$

(6.3g)
$$(\mathcal{K}_{3}\delta_{\tau}\boldsymbol{B}_{h}^{k+1}, \tilde{\boldsymbol{\varphi}}_{h}) + \varepsilon_{0}^{-1}(\boldsymbol{\mathcal{Q}}_{3}\boldsymbol{B}_{h}^{k+1}, \tilde{\boldsymbol{\varphi}}_{h}) = (\mathcal{K}_{1}\delta_{\tau}\tilde{\boldsymbol{B}}_{h}^{k+1}, \tilde{\boldsymbol{\varphi}}_{h}) + \varepsilon_{0}^{-1}(\boldsymbol{\mathcal{Q}}_{1}\overline{\tilde{\boldsymbol{B}}}_{h}^{k+1}, \tilde{\boldsymbol{\varphi}}_{h}),$$

(6.3h)
$$\mu_0(\boldsymbol{\mu}_{\infty}\delta_{\tau}\boldsymbol{H}_h^{k+1}, \hat{\boldsymbol{\varphi}}_h) + \mu_0 \sum_{l=0}^{L} (\boldsymbol{g}_l \boldsymbol{K}_{lh}^{k+1}, \hat{\boldsymbol{\varphi}}_h) = (\delta_{\tau}\boldsymbol{B}_h^{k+1}, \hat{\boldsymbol{\varphi}}_h),$$

(6.3i)
$$(\delta_{\tau} \boldsymbol{K}_{lh}^{k+\frac{1}{2}}, \boldsymbol{\varphi}_{lh}) + (\boldsymbol{\Gamma}_{ml} \overline{\boldsymbol{K}}_{lh}^{k+\frac{1}{2}}, \boldsymbol{\varphi}_{lh}) = (\boldsymbol{\omega}_{m}^{2} \boldsymbol{H}_{h}^{k+\frac{1}{2}}, \boldsymbol{\varphi}_{lh}) - (\boldsymbol{\omega}_{ml}^{2} \boldsymbol{M}_{lh}^{k+\frac{1}{2}}, \boldsymbol{\varphi}_{lh}),$$

(6.3j)
$$(\delta_{\tau} \boldsymbol{M}_{lh}^{k+1}, \tilde{\boldsymbol{\varphi}}_{lh}) = (\boldsymbol{K}_{lh}^{k+1}, \tilde{\boldsymbol{\varphi}}_{lh}),$$

which hold true for any $\psi_h, \tilde{\psi}_h, \hat{\psi}_h \in V_h^0$, $\tilde{\psi}_{qh}, \psi_{qh} \in V_h$, $\varphi_h, \tilde{\varphi}_h, \hat{\varphi}_h, \varphi_{qh}, \hat{\varphi}_{qh} \in U_h$, $q = 0, 1, \dots, Q$, and $l = 0, 1, \dots, L$.

Last, we will carry out many interesting 2D simulations. The corresponding 2D APML model can be obtained by letting $s_z = 1$ in the matrix Λ . More specifically, the 2D APML governing equations are given as follows:

$$\nabla \times H = \mathcal{K}_2 \partial_t \mathbf{D} + \varepsilon_0^{-1} \mathcal{Q}_2 \mathbf{D}, \quad \kappa_x \partial_t \tilde{B} + \varepsilon_0^{-1} \sigma_x \tilde{B} = -\nabla \times \mathbf{E},$$

$$\partial_t \tilde{B} = \kappa_y \partial_t B + \varepsilon_0^{-1} \sigma_y B,$$

$$\mathcal{K}_1 \partial_t \mathbf{D} + \varepsilon_0^{-1} \mathcal{Q}_1 \mathbf{D} = \varepsilon_0 \varepsilon_\infty \partial_t \mathbf{E} + \varepsilon_0 \sum_{q=0}^Q \mathbf{f}_q \mathbf{J}_q, \quad \partial_t B = \mu_0 \mu_\infty \partial_t H + \mu_0 \sum_{l=0}^L g_l K_l,$$

$$\partial_t \mathbf{P}_q = \mathbf{J}_q, \qquad \partial_t M_l = K_l,$$

$$\partial_t \mathbf{J}_q + \Gamma_{eq} \mathbf{J}_q = \omega_p^2 \mathbf{E} - \omega_{eq}^2 \mathbf{P}_q, \quad \partial_t K_l + \Gamma_{ml} K_l = \omega_m^2 H - \omega_{ml}^2 M_l$$

where we denote matrices $\mathcal{K}_1 = \operatorname{diag}(\kappa_x, \kappa_y)$, $\mathcal{K}_2 = \operatorname{diag}(\kappa_y, \kappa_x)$, $\mathcal{Q}_1 = \operatorname{diag}(\sigma_x, \sigma_y)$, and $\mathcal{Q}_2 = \operatorname{diag}(\sigma_y, \sigma_x)$.

To solve the 2D APML model, we choose the following 2D RTN mixed finite element spaces on triangular elements:

$$\begin{split} &U_h = \{v_h \in L^2(\Omega) : v_h|_e \text{ is a piecewise constant, } e \in T_h\}, \\ &V_h = \{\boldsymbol{v}_h \in H(curl;\Omega) : \boldsymbol{v}_h|_e = \operatorname{span}\{\lambda_i \nabla \lambda_j - \lambda_j \nabla \lambda_i\}, i,j = 1,2,3,e \in T_h\}, \\ &V_h^0 = \{\boldsymbol{v}_h \in V_h : \boldsymbol{v}_h \times \boldsymbol{n} = 0, \text{ on } \partial \Omega\}, \end{split}$$

where λ_i , i = 1, 2, 3, are the barycentric coordinates for the triangle e.

The corresponding leapfrog finite element scheme for the 2D APML is as follows: Given proper initial approximations $\boldsymbol{E}_{h}^{0}, \boldsymbol{D}_{h}^{0} \in V_{h}^{0}, \boldsymbol{J}_{qh}^{\frac{1}{2}}, \boldsymbol{P}_{qh}^{0} \in V_{h}, H_{h}^{\frac{1}{2}}, \tilde{B}_{h}^{\frac{1}{2}}, B_{h}^{\frac{1}{2}}, M_{lh}^{\frac{1}{2}}, K_{lh}^{0} \in U_{h}, \text{ find } \boldsymbol{J}_{qh}^{k+\frac{3}{2}}, \boldsymbol{P}_{qh}^{k+1} \in V_{h}, H_{h}^{k+\frac{3}{2}}, \tilde{B}_{h}^{k+\frac{3}{2}}, B_{h}^{k+\frac{3}{2}}, K_{lh}^{k+1}, M_{lh}^{k+\frac{3}{2}} \in U_{h}, \boldsymbol{E}_{h}^{k+1}, \boldsymbol{D}_{h}^{k+1} \in V_{h}^{0}, \text{ such that the equations}$

(6.4a)
$$(K_2 \delta_\tau \boldsymbol{D}_h^{k+\frac{1}{2}}, \psi_h) + \varepsilon_0^{-1}(Q_2 \overline{\boldsymbol{D}}_h^{k+\frac{1}{2}}, \psi_h) = (\nabla \times \psi_h, H_h^{k+\frac{1}{2}}),$$

(6.4b)
$$(\delta_{\tau} \boldsymbol{P}_{qh}^{k+\frac{1}{2}}, \tilde{\boldsymbol{\psi}}_{qh}) = (\boldsymbol{J}_{qh}^{k+\frac{1}{2}}, \tilde{\boldsymbol{\psi}}_{qh}),$$

(6.4c)
$$(\delta_{\tau} \boldsymbol{J}_{qh}^{k+1}, \boldsymbol{\psi}_{qh}) + (\boldsymbol{\Gamma}_{eq} \overline{\boldsymbol{J}}_{qh}^{k+1}, \boldsymbol{\psi}_{qh}) = (\boldsymbol{\omega}_{p}^{2} \boldsymbol{E}_{h}^{k+1}, \boldsymbol{\psi}_{qh}) - (\boldsymbol{\omega}_{eq}^{2} \boldsymbol{P}_{qh}^{k+1}, \boldsymbol{\psi}_{qh}),$$

(6.4d)
$$\varepsilon_0(\boldsymbol{\varepsilon}_{\infty}\delta_{\tau}\boldsymbol{E}_h^{k+\frac{1}{2}},\tilde{\boldsymbol{\psi}}_h) + \varepsilon_0\sum_{q=0}^{Q}(\boldsymbol{f}_q\boldsymbol{J}_{qh}^{k+\frac{1}{2}},\tilde{\boldsymbol{\psi}}_h) = (K_1\delta_{\tau}\boldsymbol{D}_h^{k+\frac{1}{2}},\tilde{\boldsymbol{\psi}}_h)$$

$$+ \varepsilon_0^{-1}(Q_1 \overline{\boldsymbol{D}}_h^{k+\frac{1}{2}}, \tilde{\boldsymbol{\psi}}_h),$$

(6.4e)
$$(\kappa_x \delta_\tau \tilde{B}_h^{k+1}, \varphi_h) + \varepsilon_0^{-1} (\sigma_x \overline{\tilde{B}}_h^{k+1}, \varphi_h) = -(\nabla \times \boldsymbol{E}_h^{k+1}, \varphi_h),$$

(6.4f)
$$(\kappa_y \delta_\tau B_h^{k+1}, \tilde{\varphi}_h) + \varepsilon_0^{-1} (\sigma_y \overline{B}_h^{k+1}, \tilde{\varphi}_h) = (\delta_\tau \tilde{B}_h^{k+1}, \tilde{\varphi}_h),$$

(6.4g)
$$\mu_0(\mu_\infty \delta_\tau H_h^{k+1}, \tilde{\varphi}_h) + \mu_0 \sum_{l=0}^L (g_l K_{lh}^{k+1}, \tilde{\varphi}_h) = (\delta_\tau B_h^{k+1}, \tilde{\varphi}_h),$$

$$(6.4h) \qquad (\delta_{\tau}K_{lh}^{k+\frac{1}{2}},\varphi_{lh}) + (\Gamma_{ml}\overline{K}_{lh}^{k+\frac{1}{2}},\varphi_{lh}) = (\omega_{m}^{2}H_{h}^{k+\frac{1}{2}},\varphi_{lh}) - (\omega_{ml}^{2}M_{lh}^{k+\frac{1}{2}},\varphi_{lh}),$$

(6.4i)
$$(\delta_{\tau} M_{lh}^{k+1}, \tilde{\varphi}_{lh}) = (K_{lh}^{k+1}, \tilde{\varphi}_{lh}),$$

hold true for any $\psi_h, \tilde{\psi}_h \in V_h^0$, $\psi_{qh}, \tilde{\psi}_{qh} \in V_h$, and $\varphi_h, \tilde{\varphi}_h, \tilde{\varphi}_{lh}, \varphi_{lh}, \hat{\varphi}_h \in U_h$, $q = 0, 1, \dots, Q$, and $l = 0, 1, \dots, L$.

- 7. Numerical results. Here we present some numerical results to first justify the convergence rate of our scheme (3.1), then use (6.3) and (6.4) to simulate the superresolution imaging achieved by 2D and 3D metal-dielectric multilayers hyperlenses.
- 7.1. Convergence test in the 3D case. This example is developed to test the convergence rate of our FETD scheme in the 3D case with $\Omega = [0,1]^3$, which is first divided into uniform cubes with length h, and then each cube is divided into six tetrahedra. We choose physical parameters $L=1,\ Q=2,\ \varepsilon_0=\mu_0=1,$ $\varepsilon_\infty=\mathrm{diag}(1,2,1),\ \boldsymbol{\omega}_p^2=\pi^2\mathrm{diag}(1,1,2),\ \boldsymbol{\mu}_\infty=\mathrm{diag}(3,3,2),\ \boldsymbol{\omega}_m^2=\pi^2\mathrm{diag}(1,2,1),$ and the other parameters.

\overline{q}	Γ_{eq}	$oldsymbol{\omega}_{eq}^2$	$oldsymbol{f}_q$
0	$\pi \operatorname{diag}(2,2,3)$	0	diag(2, 3, 4)
1	$\pi \operatorname{diag}(3,3,4)$	$\pi^2 \text{diag}(1, 1, 1)$	diag(2, 1, 0)
2	0	$\pi^2 \operatorname{diag}(0,0,1)$	$\operatorname{diag}(1,0,1)$
\overline{l}	Γ_{ml}	$oldsymbol{\omega}_{ml}^2$	$oldsymbol{g}_l$
0	$\pi \operatorname{diag}(2,3,2)$	0	diag(1, 0, 0)
1	$\pi \operatorname{diag}(2,4,2)$	$\pi^2 \operatorname{diag}(0,1,0)$	diag(0,1,0)

We choose an exact solution $(E, J_q, P_q, H, K_l, M_l)$ given as follows:

$$\begin{aligned} & \boldsymbol{E} = \exp(-\pi t) \begin{bmatrix} A\cos(\pi x)\sin(\pi y)\sin(\pi z) \\ B\sin(\pi x)\cos(\pi y)\sin(\pi z) \\ C\sin(\pi x)\sin(\pi y)\cos(\pi z) \end{bmatrix}, \\ & \boldsymbol{H} = \exp(-\pi t) \begin{bmatrix} (C-B)\sin(\pi x)\cos(\pi y)\cos(\pi z) \\ (A-C)\cos(\pi x)\sin(\pi y)\cos(\pi z) \\ (B-A)\cos(\pi x)\cos(\pi y)\sin(\pi z) \end{bmatrix}, \\ & \boldsymbol{J}_0 = \pi \boldsymbol{E}, \ \boldsymbol{P}_0 = -\boldsymbol{E}, \boldsymbol{J}_1 = \pi \boldsymbol{E}, \ \boldsymbol{P}_1 = -\boldsymbol{E}, \ \boldsymbol{J}_2 = -\pi \boldsymbol{E}, \ \boldsymbol{P}_2 = \boldsymbol{E}, \\ & \boldsymbol{K}_0 = \pi \boldsymbol{H}, \ \boldsymbol{M}_0 = -\boldsymbol{H}, \boldsymbol{K}_1 = \pi \boldsymbol{H}, \ \boldsymbol{M}_1 = -\boldsymbol{H}. \end{aligned}$$

This exact solution requires us to add source terms \mathbf{F}_m and \mathbf{F}_e to (2.8a) and (2.8b) as follows:

$$\begin{split} \boldsymbol{F}_{e} &= \nabla \times \boldsymbol{H} - \varepsilon_{0} \boldsymbol{\varepsilon}_{\infty} \partial_{t} \boldsymbol{E} - \varepsilon_{0} \sum_{q=0}^{Q} \boldsymbol{f}_{q} \boldsymbol{J}_{q} \\ &= -\pi \exp(-\pi t) \begin{bmatrix} (B+C) \cos(\pi x) \sin(\pi y) \sin(\pi z) \\ (C+A) \sin(\pi x) \cos(\pi y) \sin(\pi z) \\ (A+B) \sin(\pi x) \sin(\pi y) \cos(\pi z) \end{bmatrix}, \\ \boldsymbol{F}_{m} &= -\nabla \times \boldsymbol{E} - \mu_{0} \boldsymbol{\mu}_{\infty} \partial_{t} \boldsymbol{H} - \mu_{0} \sum_{l=0}^{L} \boldsymbol{g}_{l} \boldsymbol{K}_{l} = \pi \boldsymbol{H}. \end{split}$$

In our simulation, we choose A=1, B=2, C=3 and fix the time step size $\tau=h/20$ with varying mesh size h. The obtained L^2 errors at time T=1 are given in Table 1, which clearly shows the theoretical O(h) convergence rate.

 $\label{eq:table 1} \text{Table 1}$ The obtained L^2 errors at T=1 with $\tau=h/20$ in the 3D case.

$\overline{h^{-1}}$	$\ {m E}_h - {m E}\ _0$	Rates	$ oldsymbol{E}_h - oldsymbol{E} _{curl}$	Rates	$\ {m H}_h - {m H}\ _0$	Rates
4	0.670553		3.7653		1.44747	
8	0.32537	1.04327	2.23092	0.755126	0.714852	1.01782
16	0.161506	1.01049	1.09442	1.02747	0.355077	1.00951
32	0.0802587	1.00886	0.559287	0.968509	0.177003	1.00436
64	0.0400912	1.00137	0.224768	1.31515	0.0884003	1.00165

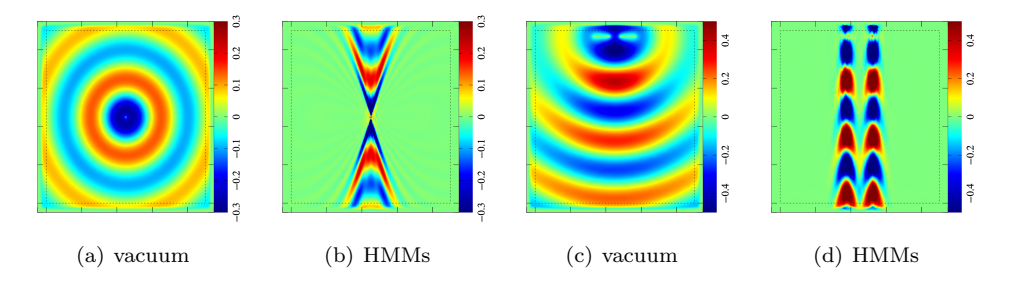


Fig. 1. (a) and (b) are the contour plots of the magnetic field at $t=3000\tau$ when the incident source wave is H_s ; (c) and (d) are the contour plots of the magnetic field at $t=4000\tau$ when the incident source wave is $H_{s,G}$.

7.2. Single frequency waves propagating in 2D ideal HMMs. In this subsection, we simulate how single-frequency waves propagate in 2D ideal HMMs. First, we take an incident source wave $H_s = \sin(\omega t)\delta(\boldsymbol{x}_c)$ imposed at point $\boldsymbol{x}_c = (1.5\lambda, 1.5\lambda)$, where $\lambda = 300$ nm and $\delta(\boldsymbol{x}_c)$ denotes the Dirac delta function. The physical domain is $[0, 3\lambda] \times [0, 3\lambda]$, and our simulation uses $h = \lambda/60$ and $\tau = 10^{-18}$ s. We use the modeling physical parameters $Q = 0, L = -1, \boldsymbol{f}_0 = \text{diag}(0, 1), \boldsymbol{\varepsilon}_{\infty} = I_2, \boldsymbol{\omega}_{e0} = \boldsymbol{0}, \boldsymbol{\Gamma}_{e0} = \boldsymbol{0}, \boldsymbol{\omega}_p = 3\omega I_2, \, \mu_{\infty} = 1, \boldsymbol{\omega} = 2\pi f \text{ with } f = C_v/\lambda \approx 999.3 \text{ THz}.$ The relative permittivity $\boldsymbol{\varepsilon}_r = \boldsymbol{\varepsilon}_{\infty} - \omega^{-2} \boldsymbol{f}_0 \boldsymbol{\omega}_p^2 = \text{diag}(1, -8)$. The simulated magnetic fields in vacuum and HMMs are shown in Figure 1(a) and (b), respectively.

Then we keep the same physical parameters as those used for Figure 1(a) and (b) except $\omega_p = 7\omega I_2$. The relative permittivity $\varepsilon_r = \varepsilon_\infty - \omega^{-2} \boldsymbol{f}_0 \omega_p^2 = \mathrm{diag}(1, -48)$. The incident source wave $H_{s,G} = \sin(\omega t) G(\boldsymbol{x})$, where $G(\boldsymbol{x}) = \exp(-\frac{|\boldsymbol{x}-\boldsymbol{x}_c|^2}{W^2})$ with $W = 0.1\lambda$, is imposed on two line segments: one from point $(1.1\lambda, 2.9\lambda)$ to point $(1.4\lambda, 2.9\lambda)$; and another one from point $(1.6\lambda, 2.9\lambda)$ to point $(1.9\lambda, 2.9\lambda)$. The simulated results in both vacuum and HMMs are shown in Figure 1(c) and (d), respectively, which clearly show that HMMs can break the optical diffraction limit. Our results are similar to those obtained in [10, Figure 2] and [14, Figure 4].

7.3. Simulation of waves propagation in 2D hyperbolic superlenses. In [27, 20], the authors showed that when the electromagnetic wave with wavelength 365 nm passes through the alumina-silver multilayer film ($\varepsilon_{Ag} = -2.4012 - 0.2488j$, $\varepsilon_{Al_2O_3} = 3.217$), the wave yields a hyperbolic dispersion, which shows that the device can realize superresolution imaging. Their conclusion is drawn through simulations via COMSOL Multiphysics under the assumption that the incident wave is single-frequency.

In our numerical experimental designs of this section, we always use the combination of one-layer dielectric film and one-layer metal film as the basic unit for the multilayer structure and denote $t_l = t_d + t_m$, where t_d and t_m are the thickness of one-layer dielectric and metal films. In our experimental designs, we fix $\alpha := t_d/t_l$.

Let ε_{\parallel} and ε_{\perp} denote the tangential and normal permittivity of the multilayers, respectively, and then the effective permittivity tensor is given by [41]:

$$\varepsilon_r = \operatorname{diag}(\varepsilon_{\parallel}, \varepsilon_{\perp}, \varepsilon_{\parallel}), \quad \varepsilon_{\parallel} = \alpha \varepsilon_d + (1 - \alpha) \varepsilon_m, \qquad \quad \varepsilon_{\perp} = \frac{1}{\alpha / \varepsilon_d + (1 - \alpha) / \varepsilon_m},$$

where ε_d and ε_m are the relative permittivity of dielectric and metal, respectively.

According to [15], the bigger conductivity σ and wave frequency ω , the smaller the skin depth δ_C of a nonmagnetic medium. Hence we would like to ensure that the metal has a negative permittivity and an electrical conductivity as low as possible.

It is known [2] that at high-frequency (or short wavelength) such as at the visible light band, the relative permittivity of aluminum oxide Al_2O_3 is almost unchanged and around 3.2. We will use the D-L model to simulate metals.

Substituting the D-L model parameters of silver (Ag) and aluminum (Al) given in [32, Table 2] into [32],

(7.1)
$$\varepsilon_r(\omega) = \varepsilon_{\infty} + \frac{f_0 \omega_p^2}{(j\omega)^2 + j\omega\Gamma_{e0}} + \sum_{q=1}^Q \frac{f_q \omega_p^2}{\omega_{eq}^2 + (j\omega)^2 + j\omega\Gamma_{eq}},$$

we obtain Figure 2.

In this subsection, we use both single-frequency wave $H_{s,G}$ and multifrequency wave $H_{G_c,G} = G_{\cos}(t)G(\boldsymbol{x})$ as incident waves, and the waist W of Gaussian beamer is always equal to half the length of the segment of the wave source. The cosine modulated Gaussian pulse $G_{\cos}(t)$ is expressed as

$$G_{\cos}(t) = \cos(\omega(t - t_0)) \exp\left(-4\pi \frac{(t - t_0)^2}{\tau_c^2}\right)$$

with effective wavelength band $[(\frac{1}{\lambda} + \frac{C_{\tau}\Delta\lambda}{\lambda^2 - (\Delta\lambda)^2})^{-1}, (\frac{1}{\lambda} - \frac{C_{\tau}\Delta\lambda}{\lambda^2 - (\Delta\lambda)^2})^{-1}]$ (i.e., the effective frequency band is $[\frac{C_v}{\lambda} + \frac{C_vC_{\tau}\Delta\lambda}{\lambda^2 - (\Delta\lambda)^2}, \frac{C_v}{\lambda} - \frac{C_vC_{\tau}\Delta\lambda}{\lambda^2 - (\Delta\lambda)^2}])$, where $C_{\tau} = \frac{2}{0.483}\sqrt{-\frac{\ln(0.8)}{\pi}}$, the fundamental angular frequency $\omega = 2\pi f_0$, the center frequency $f_0 = \frac{C_v}{\lambda}$, and

$$t_0 = 0.6\tau_c, \quad \tau_c = 0.966 / \left(\frac{C_v}{\lambda - \Delta \lambda} - \frac{C_v}{\lambda + \Delta \lambda}\right).$$

7.3.1. Aluminum oxide and silver. First, we consider aluminum oxide $(t_d = 12.5 \ nm)$ and silver $(t_m = 12.5 \ nm)$ for the lens given in Figure 3(a), with inner radius $120 \ nm$ and thickness $450 \ nm$. The center distance of the incident waves is $148.7 \ nm$. The physical area is $[0, 1365](nm) \times [0, 840](nm)$, and the PML thickness is 12h, where

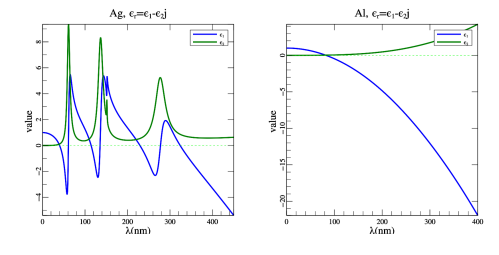
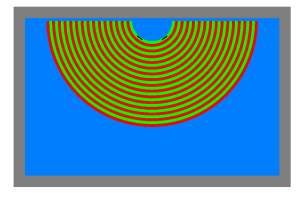
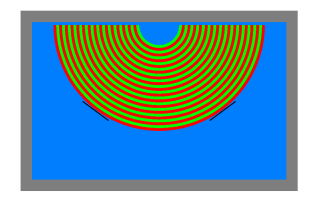


FIG. 2. The relationship between wave wavelength and the relative permittivity of silver (Ag) and aluminum (Al).

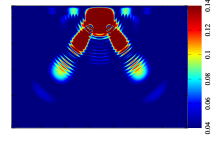


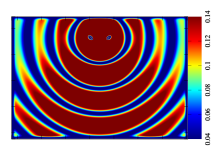


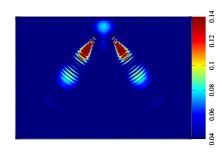
(a) t_l is independent of direc- (b) Same as (1), but the incition.

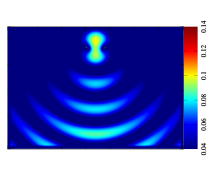
dent wave positions are differ-

Fig. 3. Sketches of two hyperbolic superlenses: the red parts represent metal, the green parts are dielectric, the black segments are the incident wave's positions, the blue parts are the background medium (vacuum), and the gray areas denote the PML. (Color images are available online.)









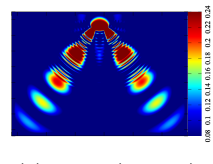
(a) 16.5fs (HMMs)

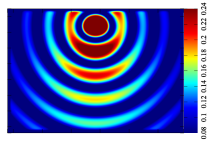
(b) 16.5fs (vacuum)

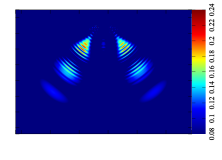
(c) 19.5 fs (HMMs)

(d) 19.5fs (vacuum)

Fig. 4. Distribution of the magnetic field intensity $|H_z|$. (1) and (2). The incident wave is $H_{s,G}$ with wavelength $\lambda=380$ nm. (3) and (4). The incident wave is $H_{G_c,G}$ with $\lambda=380$ nm and $\Delta\lambda=12$ nm. The time step τ is $1.5\cdot 10^{-18}$ s, and 1 femtosecond (fs) = $1\cdot 10^{-15}$ s.









(a) 4.9fs (HMMs)

(b) 4.9fs (vacuum)

(c) 3.85fs (HMMs)

(d) 3.85fs (vacuum)

Fig. 5. Contour plot of the magnetic field intensity $|H_z|$. (1) and (2). The incident wave is $H_{s,G}$ with wavelength $\lambda = 150 \text{ nm}$. (3) and (4). The incident wave is $H_{G_s,G}$ with $\lambda = 150 \text{ nm}$ and $\Delta \lambda = 10 \ nm$. The time step τ is $0.7 \cdot 10^{-18} s$.

the mesh size $h = \frac{25}{6}nm$. The total numbers of mesh points, elements, and edges are 94407, 187344, and 281750, respectively.

Taking the incident waves as $H_{s,G}$ and $H_{G_c,G}$, respectively, we obtain the magnetic field intensity $|H_z|$ shown in Figure 4(a) and (c). The corresponding results in vacuum are shown in Figure 4(b) and (d). Figure 4(a) and (c) are similar to 20, Figure 2 and show clearly that HMMs achieve superresolution imaging.

7.3.2. Aluminum oxide and aluminum. In this example, we consider using aluminum oxide $(t_d = 5 nm)$ and aluminum $(t_m = 5 nm)$ for the lens shown in Figure 3(a), with inner radius 35 nm and thickness 200 nm. The center distance of the incident wave is chosen as $45.4 \, nm$. The physical domain is $[0,570] \times [0,355] (nm)$, and the PML thickness is 12h. The total numbers of mesh points, elements, and edges are 102106, 202709, and 304814, respectively.

For this example, we take both $H_{s,G}$ and $H_{G_c,G}$ for the incident waves. The obtained magnetic field intensities $|H_z|$ are shown in Figure 5(a) and (c), and the corresponding results in vacuum are shown in Figure 5(b) and (d). Same superresolution imaging is achieved by the HMMs as shown by Figure 5(a) and (c).

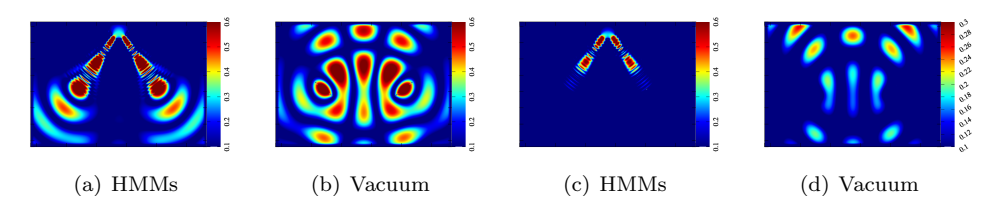


FIG. 6. Distribution of the magnetic field intensity $|H_z(3.85fs)|$. (1) and (2). The incident wave is $H_{s,G}$ with $\lambda=150$ nm. (3) and (4). The incident wave is $H_{G_c,G}$ with $\lambda=150$ nm and $\Delta\lambda=10$ nm. The time step $\tau=0.7\cdot 10^{-18}s$.

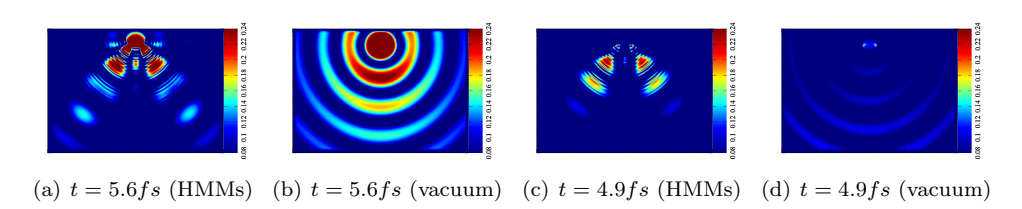


Fig. 7. Distribution of the magnetic field intensity $|H_z|$. (a) and (b). The incident wave is $H_{s,G}$ with $\lambda=180$ nm. (c) and (d). The incident wave is $H_{G_c,G}$ with $\lambda=180$ nm and $\Delta\lambda=10$ nm. The time step $\tau=0.7\cdot 10^{-18}s$.

This last example is developed to verify the photolithography of the lenses given in Figure 5(b) and is composed of aluminum oxide $(t_d = 5 nm)$ and aluminum $(t_m = 5 nm)$. The inner radius and thickness of the lenses are 24 nm and 200 nm, respectively, the center distance of the incident wave is 271.2 nm, the distance of transmitted waves at the output interface is about 28.6 nm, and the physical domain and mesh data are the same as those used for Figure 5(c). The magnetic field intensities $|H_z|$ obtained with incident waves $H_{s,G}$ and $H_{G_c,G}$ are shown in Figure 6(a) and (c), respectively. The corresponding results in vacuum are shown in Figure 6(b) and (d). Figure 6(a) and (c) are similar to [37, Figure 2(a)], and they show that this lens can be used in nanolithography.

7.3.3. Titanium (V) oxide and aluminum. This example uses titanium (V) oxide $(Ti_3O_5, \varepsilon_r = 5.85, t_d = 5\,nm)$ and aluminum $(t_m = 5\,nm)$ for the lenses shown in Figure 3(a). The inner radius and thickness of the lenses are $32\,nm$ and $200\,nm$, respectively, and the center distance of the incident wave is $40.4\,nm$. The physical domain for the simulation is $[0,564] \times [0,352](nm)$, and the PML thickness is 12h with $h = \frac{5}{3}\,nm$. The total numbers of mesh points, elements, and edges are 100404, 199310 and 299713, respectively.

The obtained magnetic field intensity $|H_z|$ for the incident waves $H_{s,G}$ and $H_{G_c,G}$ are shown in Figure 7(a) and (c), respectively. The corresponding results in vacuum are shown in Figure 7(b) and (d).

7.4. Multifrequency wave propagation in 3D hyperbolic superlenses. Now we simulate the wave propagation of multifrequency waves in a 3D cylindrical multilayer lens. We take Figure 3(a) as the xy plane cross section of the 3D cylindrical lens with inner radius $R_{inner} = 45 \ nm$ and lens thickness $8t_l$, where $t_l = 15 \ nm$. This lens is made from aluminum oxide $t_d = 7.5 \ nm$ and aluminum $(t_m = 7.5 \ nm)$. The physical domain is $[0,234] \ nm \times [0,195] \ nm \times [0,150] \ nm$, and the PML thickness is $10h \ \text{with} \ h = \frac{15}{4} \ nm$. The total numbers of mesh points, tetrahedra, faces, and edges are 691005, 4223404, 8493242, and 4960842, respectively.

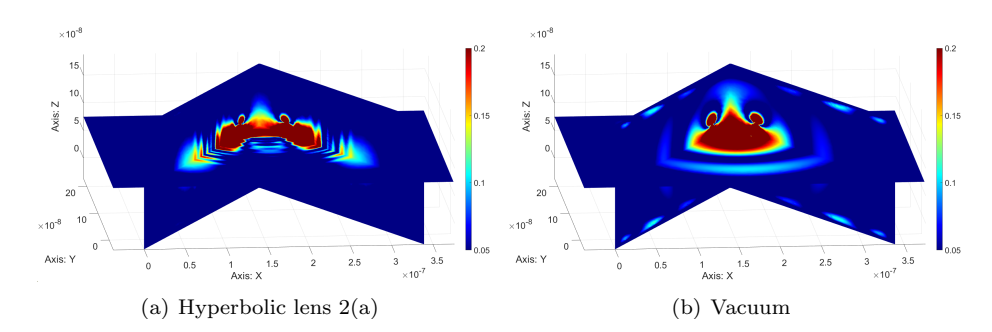


Fig. 8. Distribution of magnetic field intensity $|H_z|$ obtained with incident wave $H_{G_c,G}$ with frequency $\lambda=150$ nm and $\Delta\lambda=7$ nm passing through the lens given in Figure 3 at time $T=6000\tau$, where time step $\tau=0.6\cdot 10^{-18} s$.

Table 2

The multilayer lens' size, operating frequency, and resolution. The units of t_m , t_l , resolution S_r , and λ are in nanometers (nm).

Lens	t_m	t_d	Resolution S_r	λ	λ/S_r	Figures
Al_2O_3/Ag	12.5	12.5	148.7	[367,394]	[2.47, 2.65]	Figure 4(c)
Al_2O_3/Al	5	5	45.4	[140,162]	[3.08, 3.57]	Figure 5(c)
Ti_3O_5/Al	5	5	40.4	[170,192]	[4.20, 4.75]	Figure 7(c)

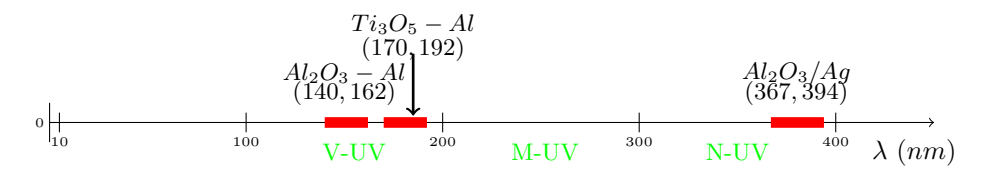


Fig. 9. Distribution of the operating frequencies of all experimental lenses in the ultraviolet band.

The multifrequency source wave is taken as

$$H_{G_c,G}^{(3D)} = G_{cos}(t) exp\left(-\frac{(x-x_c)^2 + (z-z_c)^2}{W_1^2}\right) exp\left(-\frac{(y-y_c)^2}{W_2^2}\right)$$

with widths $W_1 = 19.2 \, nm$ and $W_2 = 45 \, nm$. The source wave is imposed on quadrilaterals SP_1 and SP_2 , where SP_1 is formed by nodes (134.5, 155.1, 52.5), (150.2, 143, 52.5), (150.2, 143, 97.5), (134.5, 155.1, 97.5) with center (142.3, 149.1, 75), and SP_2 is formed by nodes (204.5, 155.1, 52.5), (188.8, 143, 52.5), (188.8, 143, 97.5), (204.5, 155.1, 97.5) with center (196.7, 149.1, 75). The obtained contour plots of magnetic field intensity $|H_z|$ are presented in Figure 8.

Finally, let us summarize our experimental data for all the above lenses in Table 2. Usually, λ/S_r is used to measure the superresolution effect of a lens. We say that the lens can achieve superresolution imaging when $\lambda/S_r > 2$. It is known that the larger λ/S_r is, the better superresolution performance the lens has. Table 2 shows that the performance of a multilayer lens made of titanium (V) oxide and aluminum (Ti_3O_5/Al) is the best among our experiments, but its resolution is not the best.

Comparing the operating wavelengths of lenses, we see that the working frequencies of different lenses are distributed in different bands of ultraviolet light (see Figure 9). For example, the operating frequencies of lenses Al_2O_3/Al and Ti_3O_5/Al are in vacuum ultraviolet (VUV: $100-200\ nm$), and the operating frequency of lenses Al_2O_3/Ag is in near ultraviolet (NUV: $300-400\ nm$).

8. Conclusion. In this paper, we derive the time-dependent Maxwell's equations in anisotropic dispersive media by using the Drude-Lorentz model. This model is composed of two PDEs supplemented with 2(Q+L+2) ODEs. We prove an energy identity and stability for this model and develop a leapfrog type finite element scheme to solve this model. Discrete stability and optimal convergence $O(\tau^2 + h)$ are established for our scheme by using the lowest-order edge element. Extensive numerical results are presented to verify the optimal convergence result and demonstrate many interesting superresolution imaging phenomena achieved by HMMs. In the future, we plan to study some efficient adaptive finite element methods with a proper posteriori error estimator to resolve the sharp transition in hyperbolic media.

Acknowledgment. The authors are very grateful to two anonymous referees for their insightful comments on improving the paper.

REFERENCES

- G. BAO, P. LI, AND H. WU, An adaptive edge element method with perfectly matched absorbing layers for wave scattering by biperiodic structures, Math. Comp., 79 (2010), pp. 1–34.
- [2] A. S. BARKER, Infrared lattice vibrations and dielectric dispersion in corundum, Phys. Rev., 132 (1963), 1474.
- [3] B. BID'EGARAY-FESQUET, Stability of FD-TD schemes for Maxwell-Debye and Maxwell-Lorentz equations, SIAM J. Numer. Anal., 46 (2008), pp. 2551-2566.
- [4] D. Boffi, P. Fernandes, L. Gastaldi, and I. Perugia, Computational models of electromagnetic resonators: Analysis of edge element approximation, SIAM J. Numer. Anal., 36 (1999), pp. 1264–1290.
- V. A. Bokil and N. L. Gibson, Analysis of spatial high-order finite difference methods for Maxwell's equations in dispersive media, IMA J. Numer. Anal., 32 (2012), pp. 926–956.
- [6] J. D. CALDWELL, A. V. KRETININ, Y. CHEN, V. GIANNINI, M. M. FOGLER, Y. FRANCESCATO, C. T. ELLIS, J. G. TISCHLER, C. R. WOODS, A. J. GILES, M. HONG, K. WATANABE, T. TANIGUCHI, S. A. MAIER, AND K. S. NOVOSELOV, Sub-diffractional volume-confined polaritons in the natural hyperbolic material hexagonal boron nitride, Nat. Commun., 5 (2014)
- [7] H. CHEN, W. QIU, K. SHI, AND M. SOLANO, A superconvergent HDG method for the Maxwell equations, J. Sci. Comput., 70 (2017), pp. 1010-1029.
- [8] Z. CHEN, Q. Du, AND J. ZOU, Finite element methods with matching and nonmatching meshes for Maxwell equations with discontinuous coefficients, SIAM J. Numer. Anal., 37 (2000), pp. 1542–1570.
- [9] B. H. CHENG, Y. Z. HO, Y.-C. LAN, AND D. P. TSAI, Optical hybrid-superlens hyperlens for superresolution imaging, IEEE J. Sel. Top. Quant. Electron., 19 (2013), 4601305.
- [10] P. CIARLET AND M. KACHANOVSKA, A mathematical study of a hyperbolic metamaterial in free space, SIAM J. Math. Anal., 54 (2022), pp. 2216–2250.
- [11] L. DEMKOWICZ, J. KURTZ, D. PARDO, M. PASZYNSKI, W. RACHOWICZ, AND A. ZDUNEK, Computing with hp-Adaptive Finite Elements, Vol. 2: Frontiers: Three Dimensional Elliptic and Maxwell Problems with Applications, 1st ed., Chapman & Hall/CRC, Baca Raton, FL, 2007.
- [12] H. Duan, Z. Du, W. Liu, and S. Zhang, New mixed elements for Maxwell equations, SIAM J. Numer. Anal., 57 (2019), pp. 320–354.
- [13] S. Gedney, An anisotropic perfectly matched layer-absorbing medium for the truncation of FDTD lattices, IEEE Trans. Antennas and Propagation, 44 (1996), pp. 1630–1639.
- [14] Z. Guo, H. Jiang, and H. Chen, Hyperbolic metamaterials: From dispersion manipulation to applications, J. Appl. Phys., 127 (2020), 071101.
- [15] B. S. Guru and H. R. Hiziroglu, Electromagnetic Field Theory Fundamentals, 2nd ed., Cambridge University Press, Cambridge, 2004.
- [16] R. HIPTMAIR, Finite elements in computational electromagnetism, Acta Numer., 11 (2002), pp. 237–340.
- [17] R. HIPTMAIR, J. LI, AND J. ZOU, Convergence analysis of finite element methods for $H(curl; \omega)$ elliptic interface problems, Numer. Math., 122 (2012), pp. 557–578.
- [18] Z. JACOB, L. V. ALEKSEYEV, AND E. NARIMANOV, Optical hyperlens: Far-field imaging beyond the diffraction limit, Opt. Express, 14 (2006), pp. 8247–8256.

- [19] S. Kruk, Z. Wong, E. Pshenay-Severin, K. O'Brien, D. Neshev, Y. Kivshar, and X. Zhang, Magnetic hyperbolic optical metamaterials, Nat. Commun., 7 (2016), 11329.
- [20] H. LEE, Z. LIU, Y. XIONG, C. SUN, AND X. ZHANG, Development of optical hyperlens for imaging below the diffraction limit, Opt. Express, 15 (2007), pp. 15886–15891.
- [21] J. LI AND J. S. HESTHAVEN, Analysis and application of the nodal discontinuous Galerkin method for wave propagation in metamaterials, J. Comput. Phys., 258 (2014), pp. 915–930.
- [22] J. LI AND Y. HUANG, Time-Domain Finite Element Methods for Maxwell's Equations in Metamaterials, Springer Ser. Comput. Math. 43, Springer, Berlin, 2013.
- [23] J. LI, Y. HUANG, W. YANG, AND A. WOOD, Mathematical analysis and time-domain finite element simulation of carpet cloak, SIAM. J. Appl. Math., 74 (2014), pp. 1136–1151.
- [24] J. LI, C.-W. SHU, AND W. YANG, Development and analysis of two new finite element schemes for a time-domain carpet cloak model, Adv. Comput. Math., 48 (2022), 24.
- [25] J. Li And A. Wood, Finite element analysis for wave propagation in double negative metamaterials, J. Sci. Comput., 32 (2007), pp. 263–286.
- [26] J. Lin, An adaptive boundary element method for the transmission problem with hyperbolic metamaterials, J. Comput. Phys., 444 (2021), 110573.
- [27] Z. LIU, H. LEE, Y. XIONG, C. SUN, AND X. ZHANG, Far-field optical hyperlens magnifying sub-diffraction-limited objects, Science, 315 (2007), 1686.
- [28] T. Lu, P. Zhang, and W. Cai, Discontinuous Galerkin methods for dispersive and lossy Maxwell's equations and PML boundary conditions, J. Comput. Phys., 200 (2004), pp. 549–580.
- [29] P. Monk, Finite Element Methods for Maxwell's Equations, Oxford University Press, Oxford, 2003.
- [30] J. C. NEDELEC, Mixed finite elements in \mathbb{R}^3 , Numer. Math., 35 (1980), pp. 315–341.
- [31] D. D. NGUYEN AND S. ZHAO, A new high order dispersive FDTD method for Drude material with complex interfaces, J. Comput. Appl. Math., 285 (2015), pp. 1–14.
- [32] A. D. RAKIĆ, A. B. DJURIŠIĆ, J. M. ELAZAR, AND M. L. MAJEWSKI, Optical properties of metallic films for vertical-cavity optoelectronic devices, Appl. Opt., 37 (1998), pp. 5271– 5283.
- [33] P. A. RAVIART AND J. M. THOMAS, A mixed finite element method for 2-nd order elliptic problems, in Mathematical Aspects of Finite Element Methods, Lecture Notes in Math. 606, I. Galligani and E. Magenes, eds., Springer, Berlin, 1977, pp. 292–315.
- [34] A. SALANDRINO AND N. ENGHETA, Far-field subdiffraction optical microscopy using metamaterial crystals: Theory and simulations, Phys. Rev. B, 74 (2006), 075103.
- [35] J. Schilling, Uniaxial metallo-dielectric metamaterials with scalar positive permeability, Phys. Rev. E, 74 (2006), 046618.
- [36] M. G. Silveirinha, Nonlocal homogenization model for a periodic array of ϵ -negative rods, Phys. Rev. E, 73 (2006), 046612.
- [37] J. Sun and N. M. Litchinitser, Toward practical, subwavelength, visible-light photolithography with hyperlens, ACS Nano, 12 (2018), pp. 542–548.
- [38] J. Sun, N. M. Litchinitser, and J. Zhou, Indefinite by nature: From ultraviolet to terahertz, ACS Photonics, 1 (2014), pp. 293–303.
- [39] A. TAFLOVE AND S. C. HAGNESS, Computational Electrodynamics: The Finite-Time Domain-Method, 3rd ed., Artech House, Norwood, MA, 2005.
- [40] B. WANG, Z. YANG, L.-L. WANG, AND S. JIANG, On time-domain NRBC for Maxwell's equations and its application in accurate simulation of electromagnetic invisibility cloaks, J. Sci. Comput., 86 (2021), pp. 1–34.
- [41] B. WOOD, J. B. PENDRY, AND D. P. TSAI, Directed subwavelength imaging using a layered metal-dielectric system, Phys. Rev. B, 74 (2006), 115116.
- [42] W. YANG, J. LI, AND Y. HUANG, Mathematical analysis and finite element time domain simulation of arbitrary star-shaped electromagnetic cloaks, SIAM J. Numer. Anal., 56 (2018), pp. 136–159.
- [43] J. YAO, X. YANG, X. YIN, G. BARTAL, AND X. ZHANG, Three-dimensional nanometer-scale optical cavities of indefinite medium, Proc. Natl. Acad. Sci. USA, 108 (2011), pp. 11327– 11331.
- [44] Y. ZHANG AND D. GE, Highly stable FDTD method for complicated dispersive medium, J. Xidian Univ., 45 (2018), pp. 118–123.